Mon. Not. R. Astron. Soc. **277**, 820–844 (1995)

The APM Proper Motion Project – II. The lower proper motion stars

Dafydd Wyn Evans and Mike Irwin
Royal Greenwich Observatory, Madingley Road, Cambridge CB3 0EZ

Accepted 1995 June 14. Received 1995 May 30; in original form 1994 May 13

ABSTRACT

Results are presented from the Automated Plate Measuring (APM) Proper Motion Project. The proper motions are measured from APM scans of Palomar Observatory sky survey and UK Schmidt plates. Details are given regarding the reduction of the data and the removal of systematic errors. The project covers a total sky area of almost 100 $\deg^2$ and has astrometry and photometry for $\sim 170\,000$ stars. The overall accuracy of the proper motions is shown to be 5 mas yr^{-1}, with an error in the absolute zero point of 0.6 mas yr^{-1}. Values for the solar motion and differential Galactic motions are presented. Measurements of the red stars yield values of $A = 19 \pm 6$ and $B = -13 \pm 6$ km s^{-1} kpc^{-1} for the Oort constants. A rotational shear of -21 ± 7 km s^{-1} kpc^{-1} in the z direction for the disc stars was also observed.

Key words: methods: data analysis – astrometry – Galaxy: kinematics and dynamics.

1 INTRODUCTION

Measurement of the absolute proper motions of stars provides a fundamental means of studying the local dynamical structure of the Galaxy. This requires the accurate measurement of the position of stars with reference to a coordinate frame defined by distant galaxies. Using the Automated Plate Measuring (APM) machine at Cambridge, we are able to measure the positions of more than 30 000 galaxies uniformly spread over a plate in addition to all the stars. This allows us to remove many of the systematic effects that have plagued work of this kind in the past. The removal of systematic positional errors (residuals remaining after plate matching) from the data is one of the most important aspects of the project. These errors can broadly be divided into two groups.

First, those astrometric errors that are solely dependent on the position of the object on the plate. These errors include those due to plate deformation, when the plate is forced to take the shape of the focal plane within the Schmidt telescope, and various systematic x–y table errors which manifest themselves due to objects on different plates being at physically different positions on these plates. The effects of differential refraction by the atmosphere also fall into this category, but are also a slight function of the colour of an image. Most of these errors are removed by a simple 'measurement and subtraction' technique.

The second type of astrometric errors are dependent on the physical properties of the images in question. Among these errors are the shifts due to the variation of atmospheric refractivity with image colour and the magnitude-dependent errors caused by optical aberrations of the telescope, differential saturation effects of the emulsion and possible magnitude-dependent measuring errors introduced by the APM. Even though these errors are generally smaller than the first type, care must be taken when trying to remove them since they can mimic shifts which are astronomical in origin. In addition to the magnitude and colour of the object, these errors will also be dependent on plate position.

While in Paper I (Evans 1992) stars with high proper motions were discussed, this paper deals with the remaining stars, the vast majority, which have proper motions less than 0.04 arcsec yr^{-1}. With high-proper-motion stars the proper-motion errors are small in comparison to the size of the proper motions, generally less than ~ 10 per cent. Here, the random errors are comparable in magnitude to the proper motions themselves and are therefore much more important. Similarly, the systematic errors, which are of order 0.6 mas yr^{-1}, are also important and are the limiting factors in this part of the project.

The reduced proper motions (RPM) of the low-proper-motion stars are investigated along with the effects of measuring errors on the data. It is shown that in comparison to the RPM work of Paper I, the data is more difficult to interpret. This is because of the larger relative errors.

By investigating the average proper-motion components as a function of photometric parallax in the four fields of the project it is possible to measure many of the kinematic properties of nearby stars. From the gradients of these plots, the direction and magnitude of the Solar motion can be measured and from the zero points it is possible to measure the constants of differential Galactic motion. The analysis of the motions of the red, $(O-E)>2.0$ [$(B-V)\gtrsim 1.2$], stars is straightforward, with the only modification to the Lindblad–Oort model being a velocity shear as a function of height above the Galactic plane, similar to that found by Murray (1986) in the South Galactic Pole.

Analysis of the bluer stars, however, is much more complicated. With this sample of stars there is a mixture of populations and luminosity types present. Since each of the populations has different kinematic properties, the average proper motion as a function of distance will no longer be a simple function but will depend on the ratios of these populations as a function of distance.

The proper-motion dispersion of red stars as a function of distance is also investigated. Using a simple model, based on Strömberg drift to account for the Murray z shear, it is possible to qualitatively account for the distance dependence of the proper-motion dispersion.

The measured proper motions of quasi-stellar objects (QSOs) in the 8- and 12-h fields are briefly considered in order to verify the error estimates.

2 THE DATA

For this project, four widely separated fields in areas of low Galactic obscuration were chosen. The positions for these four fields are given in Table 1. For more details and a full list of plates see Evans (1989).

The positions and intensities of all images were measured with the APM in image parameter mode. For more details see Kibblewhite et al. (1984) or chapter 2 of Evans (1988). Image classification was carried out using various APM image parameters, again see Evans (1988) for details regarding the reliability of these classifications. In general for these scans, the classification into morphological types, i.e. stars and galaxies, has an error rate of about 10 per cent, i.e. about 10 per cent of stars are classified as galaxies and 10 per cent of galaxies are classified as stars.

Each plate is scanned twice. The second time the plate is rotated by 180°. This eliminates certain systematic errors that might arise due to the measuring process. The positions are then the average for the 0° and 180° scans of each plate. The primary epoch plates are the red Palomar (E) plates, while the secondary ones are the UKST J plates. The exception to this is the 8-h field, in which the primary epoch plate is the blue Palomar plate (O62). The reason for this is that the red plate, E62, has larger (unexplained) positional errors than normal. The secondary epoch plate for the 8-h field is J6814.

In order to match all plates of a field on to the reference (J) plate a simple linear model was used. With this six-parameter transformation we can cope with shifts, rotations and expansions, and so, to first order, remove the effects of differential refraction, different plate scales, rotation of plates, etc. The matching was done in three passes. A preliminary pass using the brightest hundred or so images was carried out in order to match the two coordinate systems roughly. This was done iteratively, with the search radius being reduced progressively. These iterations were stopped when a stable initial transform was found. On the second pass, the brightest 5 per cent of images were matched using a relatively large search radius. This produced an improved transform with which the matching of all objects was carried out on the third pass. For this project, the third pass search radius was set to ~10 arcsec and naturally defined an upper proper-motion limit to the samples.

Colour and magnitude information was measured from the red and blue POSS images and calibrated using CCD images taken on the 1-m SAAO telescope. The photometric accuracy of the final data was 0.09 mag for both O and E and 0.12 for colour, $(O-E)$. The error in the colour zero point was estimated to be 0.05 mag. The CCD sequences used in the calibration can be found in Evans (1989) along with further details about the synthetic colour–colour transformations.

Table 1. This shows the positions of the four fields used in the project. The baseline for each field is also given along with the total absorption in V (Burstein & Heiles 1982) that was used throughout the paper.

Name	RA		dec		l	b	baseline	A_V
	h	m	°	′	°	°	years	
8 Hour Field	8	53	17	30	210	35	31.0	0.05
11 Hour Field	11	12	-20	00	274	37	22.1	0.10
12 Hour Field	12	05	11	30	268	71	27.1	0.00
15 Hour Field	15	00	0	00	357	48	22.9	0.15

3 POSITION-DEPENDENT ASTROMETRIC ERRORS

Normally when a plate is measured in the APM it is held horizontally and supported along all four edges. The original plates are quite thin (1 mm thick for an original cf. 3 mm for a copy plate) and will sag in the middle due to the effect of gravity. For originals this sag is ~1 mm, which causes typical systematic changes in the position of an object of about 2 μm. For glass copies the sag is almost negligible because of the greater thickness of the glass (the corresponding numbers are ~0.05 mm for the sag and the typical change in position is only ~0.005 μm). This assumes that the alignment of the APM laser is exactly normal to the plate. The alignment can be out by typically to ~1° which for a 1-mm sag can cause a shift of around 20 μm. To first order these changes in position are accounted for by the linear expansion terms in the plate matching. The second-order terms depend on the precise shape into which the plate deforms and will cause uncorrected shifts of the order of a few μm. For glass copies the second-order terms are negligible. In order to minimize this effect, original plates are placed on top of a clear sheet of glass that is 6 mm thick, in order to provide a flat supportive surface. A layer of nonane, which has the same refractive index as glass, is introduced between the plate and the sheet of glass in order to prevent interference fringes (Newton's rings) being seen. This procedure is only carried out for original plates. With copy plates and some of the earlier scans of original plates (which were not supported by a glass sheet) the shifts due to sagging are still present and their correction is discussed in Section 4.

When a plate is placed within a Schmidt telescope it is either mechanically clamped (POSS) or vacuum clamped (UKST) so that it takes the shape of the focal plane. When the plate is restored to its normal state, the position of the images will be displaced slightly due to the stresses, which were within the glass and emulsion when it was held in the telescope, being released. The amount of this displacement is dependent on the elastic properties of the glass, and it has been shown theoretically by Shepherd (1953) that all that is required is a cubic radial correction. He estimated that the size of this effect would be about 1 arcsec (15 μm) at the edge of a plate. Unfortunately we cannot use these corrections directly since some of the assumptions made are invalid, e.g. the fact that the plate remains elastic. Andersen (1971) showed that a cubic radial correction was required when he investigated the performance of the Brorfelde Schmidt telescope, so some form of correction is required for the data used in this project. Further work has been done recently on the systematic astrometirc errors of Schmidt plates. By effectively co-adding many plates it is possible to show the systematic errors caused by incorrectly clamped plates (Irwin 1994).

Since the emulsion expands to about twice its normal thickness when it is being developed, it is expected that some large-scale shifts in the emulsion will be present owing to e.g. uneven drying of the plate.

Another type of positional error is due to the mechanical design of the APM scanner. The scanning axes are defined by linear Schneeberger bearings and the loading on the balls is such that they are elastically deformed to be in contact with the ways. The table is driven using a DC motor coupled on to a ball screw which in turn is connected to the table through a backlash-free nut. This ball screw can cause an error (in x and/or y) which is periodic along one or both of the axes. Fig. 1 shows an example of this wobble. On average the amplitude of this effect is 1.5 μm, while the 'wavelength' is about 2.0 cm which corresponds to the pitch of the ball screws along the x and y axes.

Because the field of view of a Schmidt telescope is large (6×6 deg^2 in this case), differential refraction will become a problem with long exposures. The amount of refraction through the atmosphere is different for stars at the north and south ends of a plate. This effect would not be seen if the zenith distance remained the same throughout the exposure, since the effect of differential refraction is to compress the scale in the vertical direction. Note that this is not the same as the north–south direction on the plate. This sort of compression would be accounted for by the plate matching. However, during an exposure the zenith distance changes, thereby altering the amount of compression, and also the direction of the vertical changes with respect to the coordinate axes of the plate. Therefore the net result that the apparent position of a star changes as the exposure is made. The size of this effect increases the more distant the star is from the guide star (usually near the plate centre). On the plate this is seen as trailed images. Examples of the various patterns seen are found in Bowen (1967).

A large part of this effect is a rotational component which can be compensated for by adjusting the polar axis alignment of the telescope (Hinks 1898). This procedure is carried out successfully at the UK Schmidt telescope (Wallace & Tritton 1979), but as pointed out in that paper, when the zenith distance is large (~60°) the trailing patterns have large non-rotational components and in these cases differential refraction is not compensated for by a simple field rotation. For a one-hour exposure, trails of up to 4 arcsec can remain.

4 THE REMOVAL OF POSITION-DEPENDENT ASTROMETRIC ERRORS

The correction of the systematic positional errors is carried out using a simple 'measurement and subtraction' technique. This is performed both for one and two dimensions, i.e. the errors are binned in rows (and columns) along the plate in the first case and by square sections in the second. It must be emphasized that this does *not* improve the absolute positional accuracy of an object. The absolute positions on the reference plate will still be subject to the effects mentioned in

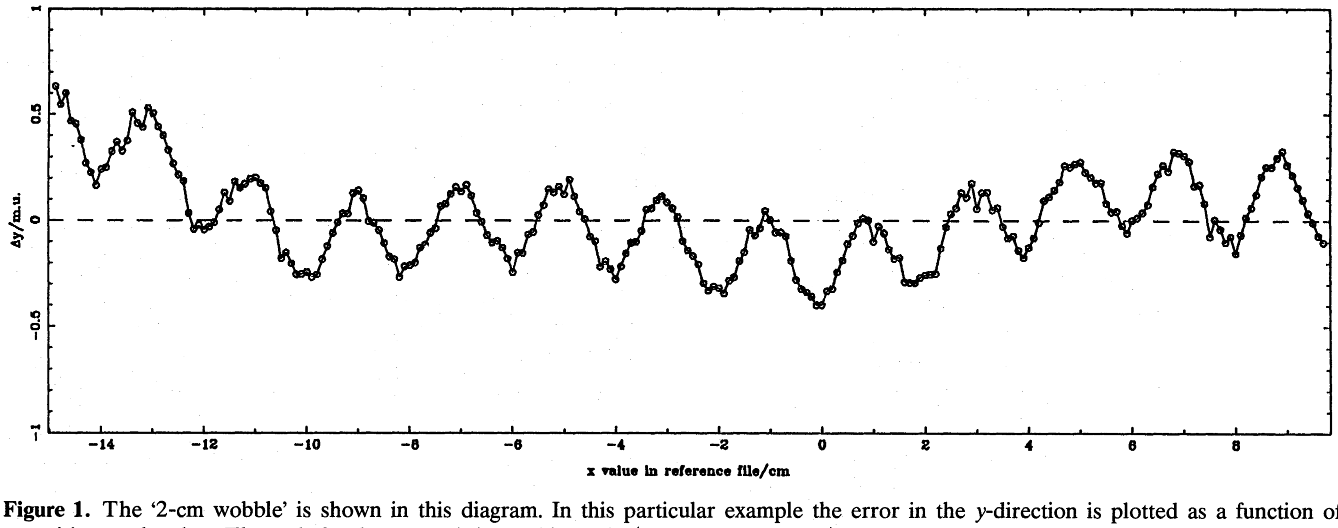

Figure 1. The '2-cm wobble' is shown in this diagram. In this particular example the error in the y-direction is plotted as a function of x-position on the plate. The scale for the y error is in machine units (= 8 μm ~ 0.5 arcsec).

the previous section and will typically be in error by ~1 arcsec. What this technique does do is remove the differential systematic errors in the positions. This is, of course, important for estimating the proper motions of objects. The basic assumption made is that the proper motion of a star is independent of its position on the plate. The absolute value of the average proper motion of all stars on the plate is determined by using the positions of all galaxies on the plate as an absolute reference frame.

The flowchart (Fig. 2) summarizes the algorithm used to remove the position-dependent astrometric errors. The letters in the flowchart refer to sections of the following text.

(a) First, a two-dimensional error mapper is applied to the data. The plate is divided into a 20×20 grid and the mean shift in x and y (caused by both systematic error and proper motion) between the reference and comparison data is calculated for each of the 400 elements in this grid. Only stars are used in this measurement. A 3×3 linear filter is applied to the two arrays (one for x shifts and the other for y shifts) to reduce noise in the error function. Using bilinear interpolation, a corrective x and y shift for each object on the plate (stars and galaxies) is calculated from this error function. This procedure will remove errors which vary over a length-scale greater than about 4 cm on the plate.

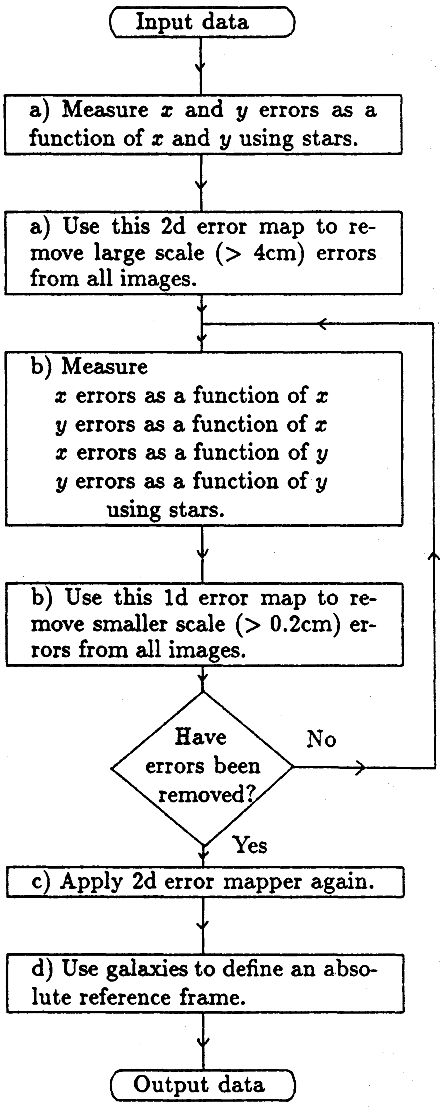

Figure 2. This flowchart shows the algorithm used to remove the position-dependent astrometric errors. The letters on the flowchart refer to sections in the text.

(b) Next, an iterative one-dimensional error mapper is used to remove errors which are dependent on either x or y, but not on products of both x and y. This procedure will remove errors with length-scales greater than about 0.5 cm. To map the errors of the whole plate, four one-dimensional functions are required: x errors as a function of x, y errors as a function of x, etc. These functions are calculated by dividing the plate into strips 0.2-cm wide and finding the mean shift in position for stars in that strip. As in part (a) these error functions are filtered before applying them to the data. A median filter of length three is first applied to remove any 'spikes' in the functions and then a linear filter of length three is used to reduce the noise. Again the corrections are interpolated from the error functions and applied to both stars and galaxies. Since these functions are not entirely independent of each other, owing to the horizontal strips crossing the vertical ones, this scheme is carried out iteratively.

(c) After the error functions have converged to zero, the two-dimensional error mapper is applied again to ensure that no residual shifts are left in the data. At this stage of the algorithm the mean 'proper motion' of all stars is zero, while that of all galaxies is non-zero.

(d) The final stage of this algorithm is to use all the galaxies on the plate to define an absolute reference frame, thus providing a well-defined zero point for the proper motions. This can be done since galaxies are so far away that they have no appreciable proper motion. The method of defining this reference frame is similar to that of the matching of the plates. The comparison data set positions of all galaxies are matched on to the reference positions using a least-squares fit to find the constants of the linear plate model. This transformation is then applied to both galaxies and stars, thus 'restoring' the mean proper motion for stars and setting that for galaxies to be zero.

The most convenient way of displaying the systematic errors that are position dependent is in the form of a 'lollipop' diagram. In this diagram the mean errors of a section of the plate are displayed in the form of a vector with a circle at one end indicating the position of the section on the plate. A linear filter is also applied to reduce the noise. Fig. 3 shows a typical example of this type of plot. Here the data is shown before any error removal has been carried out and the main error that is seen is due to differential refraction. The magnitude of these errors are of order a few arcsec. The reason that these swirling patterns are not exactly the same as those expected for differential refraction is that a linear transform has been used to match the data from the two plates. This results in there being no average shift, rotation nor expansion between the data sets, and in the alteration of the error pattern that is seen. Fig. 4 shows a lollipop diagram of a data set after large-scale error removal, but before part (d) of the algorithm. No large positional systematic error remains at this stage.

An estimate of the error in systematic mapping can be made from the equation $\varepsilon = \sigma_s/(3\sqrt{n_b})$, where σ_s is the rms half-width of the proper-motion distribution for stars (this can contain a contribution owing to the stellar velocity

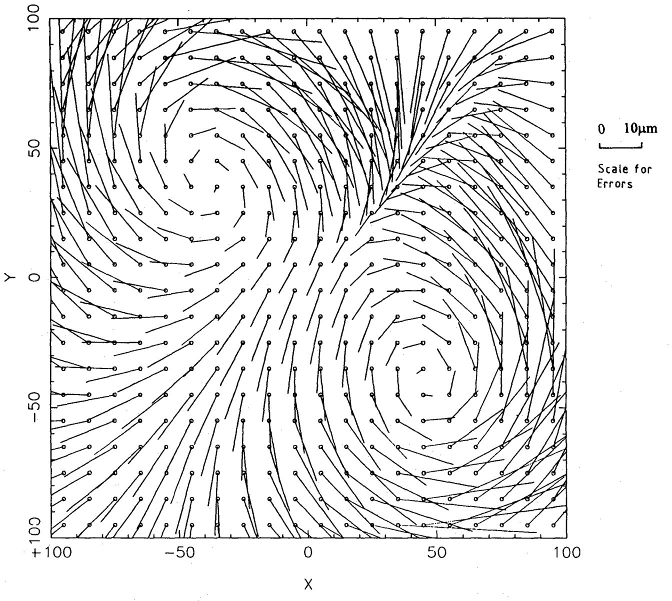

Figure 3. This diagram shows the positonal errors as a function of plate positon. The vector at each circle represnts the magnitude and direction of the average error for that section of the plate. No error removal has been carried out at this stage. The x and y scales are arbitrary, but the extent of the axes represents the total area scanned. The data shown here comes from the J and E plates of the 11-h field.

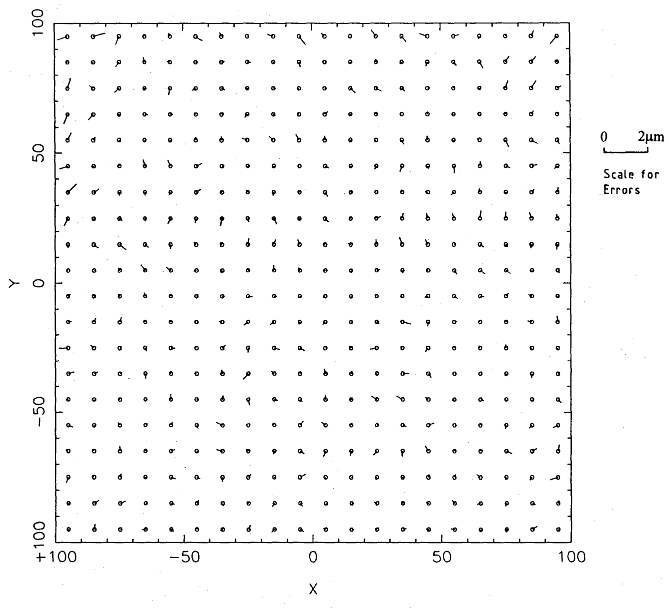

Figure 4. This diagram shows the same data as in the previous diagram after large-scale error removal. Note the change in scale for the error vectors. No large-scale positional systematic error remains at this stage.

dispersion) and n_b is the number of stars in each bin. The factor of 3 is due to the 3×3 linear filter used. With typical values of $\sigma_s = 3.5$ μm and $n_b = 120$, the error in systematic mapping is ~ 0.1 μm (~ 0.007 arcsec).

It was mentioned earlier in this section that the main assumption made in this algorithm is the independence of proper motion as a function of plate position and that any such variation is therefore due to a systematic error. This will not necessarily always be the case, since the field of view of a Schmidt telescope is quite large (6×6 deg^2). For example, close to the Galactic plane, the fraction of spheroid stars present will vary significantly with Galactic latitude. Since spheroid stars have different kinematic properties to the rest of the stars (disc), there will be a change in the mean stellar proper motion across the plate. This change will be quite small and can be approximated by a linear function across the plate. Although part (a) of the algorithm (two-dimensional error mapping) has 'removed' this change across the plate – setting stellar proper motions to zero – it has also been applied to galaxies, therefore giving them a 'pseudo proper motion'. Thus, when part (d) is carried out (establishing the extragalactic reference frame) and since the transformation used is linear, these proper-motion changes across the plate will be removed from the galaxies and restored to the stars.

Another point to note, related to this change of proper motion across the plate, is that when the proper motion of a group of stars (defined by colour and magnitude limits) is measured, it is the mean of all stars on the plate that is taken, and if there is any linear change across the plate this value will correspond to the proper motion appropriate for the centre of the plate.

If the positional errors, as a function of x-position on the plate, are binned very finely (say every 0.02 cm) and a Fourier transform carried out, the resulting power spectrum shows a peak at ~ 1 mm. This corresponds to the width of a scanning lane (128×7.6 μm). Figs 5 and 6 show an example of the power spectrum before and after the large-scale systematic errors have been removed. To display the form of this error, it is necessary to carry out the binning with respect to the position within the scanning lane (see Fig. 7). This ensures that the measurement of the effect is not affected by binning over more than one lane due to the scanning axes not being exactly parallel to the coordinate axes. In order to improve the signal-to-noise ratio, the data from all the scanning lanes on a plate are added together to form an average.

This distortion arises because, while the laser beam is scanning across each lane in the x-direction, the x–y coordinate table is continuously moving in the y-direction. In order for the x and y axes within each scanning lane to be perpendicular, as seen by the moving plate, the optical x-axis is aligned so that it is tilted slightly from the perpendicular so that the axes are orthogonal for raster scanning speed. Since the image scanning speed is different, and some error is involved in this alignment procedure, an error in y-position which is a linear function of x-position within a lane will be seen. At a lane boundary, since the laser is at a different point in its scanning pattern, there will be a discontinuity in the y error. The overall effect is to produce an error in the form a sawtooth function as seen in Fig. 7. Note that in this diagram, the zero of the x-axis has been defined at an arbitrary point within the scanning lane (hence the discontinuity does not occur at the ends) and the average error will be zero owing to the large-scale error removal that has already been carried out.

The peak-to-peak size of this error ranges from 1.5 to 4.0 μm corresponding to residual alignment errors of

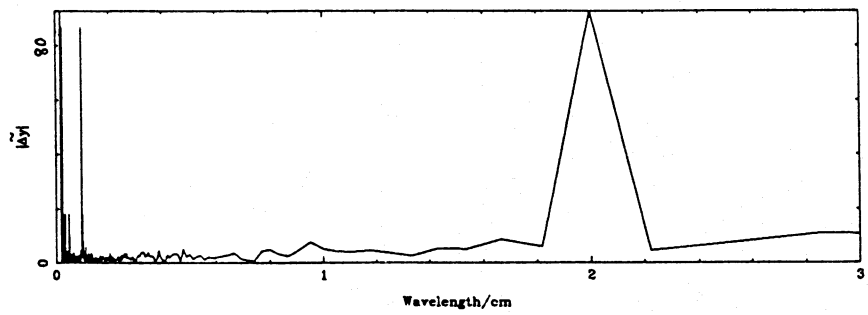

Figure 5. This diagram shows an example of the square root of the power spectrum of the positional errors (Δy in this case) as a function of x position on the plate. This has been carried out *before* any systematic errors have been removed. The '2-cm wobble' is easily seen.

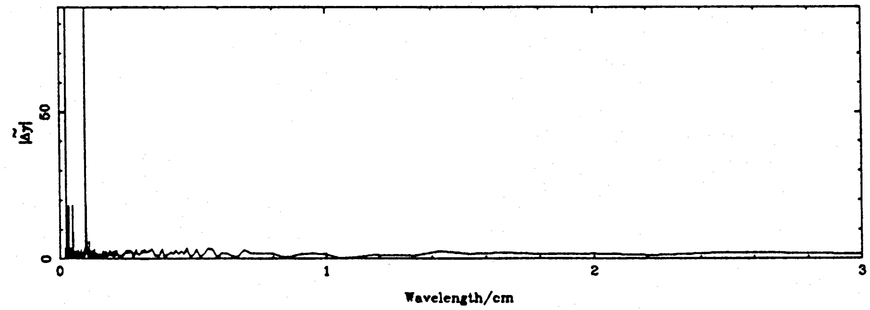

Figure 6. The same as Fig. 5 except this is *after* the large-scale positional errors have been removed. The 1-mm periodic error can be seen.

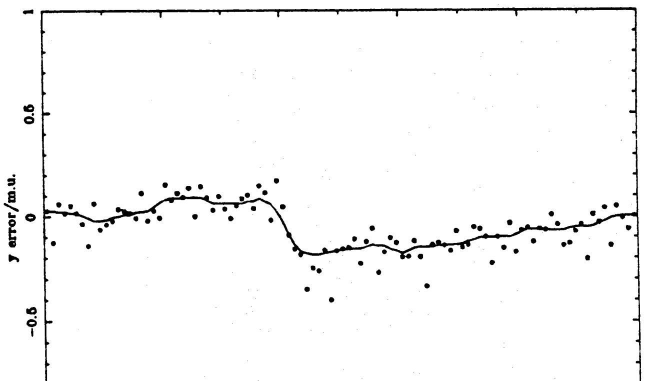

Figure 7. This diagram shows the form of the 1-mm periodic error. The data has been binned with respect to position within a scanning lane cf. Fig. 1 where the errors were binned with respect to position on the plate as a whole.

0°10–0°25. Since the position of a star within a scanning lane is random, the overall effect of this error is to increase the random error in measurement. Usually the overall y errors were more than twice as large as the x errors. After these errors have been corrected, the error distributions in x and y are approximately the same size.

The accuracy of establishing the absolute proper-motion reference frame is given by $\sigma_g/(\Delta t\sqrt{N_g})$, where σ_g is the error in measuring the change in position of a galaxy between two plates, N_g is the number of galaxies used in setting the reference frame and Δt is the baseline over which the proper motions are measured. For the four different fields, the range of errors is $0.29 < \sigma_g < 0.37$ arcsec and the number of galaxies is $8000 < N_g < 18\,000$. The baselines range from 22 to 31 yr. This corresponds to a range of zero-point error (in mas yr^{-1}) of $0.08 < \sigma_{zero} < 0.18$. With this level of accuracy, and considering the plate material available, in particular their galactic coordinates and the magnitude of the effect of differential galactic rotation, it should be possible to measure Oort's constants to an accuracy of 5–10 per cent. This is an optimistic estimate since it does not take into account other systematic errors, such as atmospheric dispersion and other photometrically dependent measuring errors.

One of these systematic errors arises from the misclassification of stars and galaxies. When calculating the average position of all galaxies, an error is made due to the galaxy sample being contaminated by 13 per cent stars (see table 2.1 of Evans 1988). Since the level of contamination is known, a correction can be made for this systematic error. Details of this calculation are given in Evans (1988).

5 PHOTOMETRICALLY DEPENDENT ASTROMETRIC ERRORS AND THEIR REMOVAL

The astrometric errors that are photometrically dependent can be easily categorized into two types. There are the recording or plate errors and there are the measuring or machine-induced errors. While the first type of error can be difficult to remove, the second type can be treated quite easily.

It was mentioned in Section 2 that plates which are to be used for astrometric measurements are scanned twice, once the 'correct' way up and once rotated by 180° to this. The position of a star is then taken as the average of the two scans. The reason for this duplication is to eliminate possible machine-induced astrometry errors which are a function of magnitude and classification. Similar errors are described in Murray & Nicholson (1975) and van Altena & Auer (1975). The reasons for this project using 0°/180° averaging are different to those described in König (1962) where the errors are physiological in nature, owing to the centring of an image on cross-hairs by eye, and are not applicable to these machine-measured positions.

An error of this type could be caused by time delays within the analogue to digital converter (ADC) which is within the APM scanner. As the laser beam scans across a bright star the intensity changes very rapidly and it is possible that, owing to the time delay mentioned, the calculated position (intensity weighted) will be shifted across in x. For a faint star or galaxy the intensity changes are more gradual, hence the effect of the time delay will be smaller. Since this effect always produces a shift in the same direction, as seen by the scanner, 0°/180° averaging will remove this error. It is expected, however, that these errors for the APM will be negligible due to the high speed of the ADC circuitry used.

Another error which produces magnitude-dependent errors is caused by the vertical misalignment of the laser beam, which is in error by typically 1°. This would not matter if the emulsion were an infinitely thin plane, but since it has a thickness of ~ 25 μm, a systematic effect will be introduced between bright stars (<17 mag) and low surface brightness objects such as galaxies and faint stars (see Fig. 8). For a bright star, the emulsion has been sensitized all the way through (i.e. it is saturated) but for faint images it is only the 'surface' of the emulsion that has been sensitized. This will cause a maximum shift between these objects of $\sim(d/2)\tan\theta$, where d is the thickness of the emulsion and θ is the vertical alignment error. For the typical values already mentioned this shift can amount to 0.2 μm. Again, 0°/180° averaging will remove this error.

For the removal of both these errors it is extremely important for the 0° and 180° scans to be taken straight after each other in order to minimize the risk of some change occurring within the scanner. The measured shifts between faint (21 mag) and bright (<17 mag) images are usually in the range 0–0.25 μm, agreeing with the estimate of the biggest shift. This error is only expected to change when the optics of the scanner are realigned. By comparing the data for all the scans, it can be shown that the alignment error is constant between realignments.

As a more direct test of the data, the difference in stellar positions between the O and E plates for each field was plotted as a function of magnitude. An example of this type of plot is shown in Fig. 9. In a large number of cases a significant systematic error as a function of magnitude was found. Table 2 lists the gradient of a linear fit to these errors for the O and E plates from the project and two other combinations

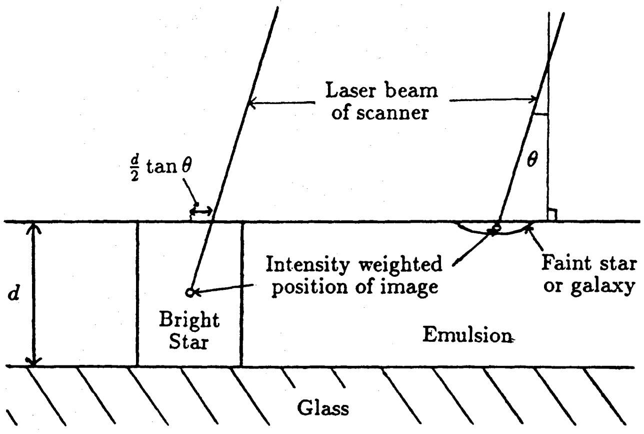

Figure 8. This drawing illustrates the error caused by the vertical misalignment of the laser beam.

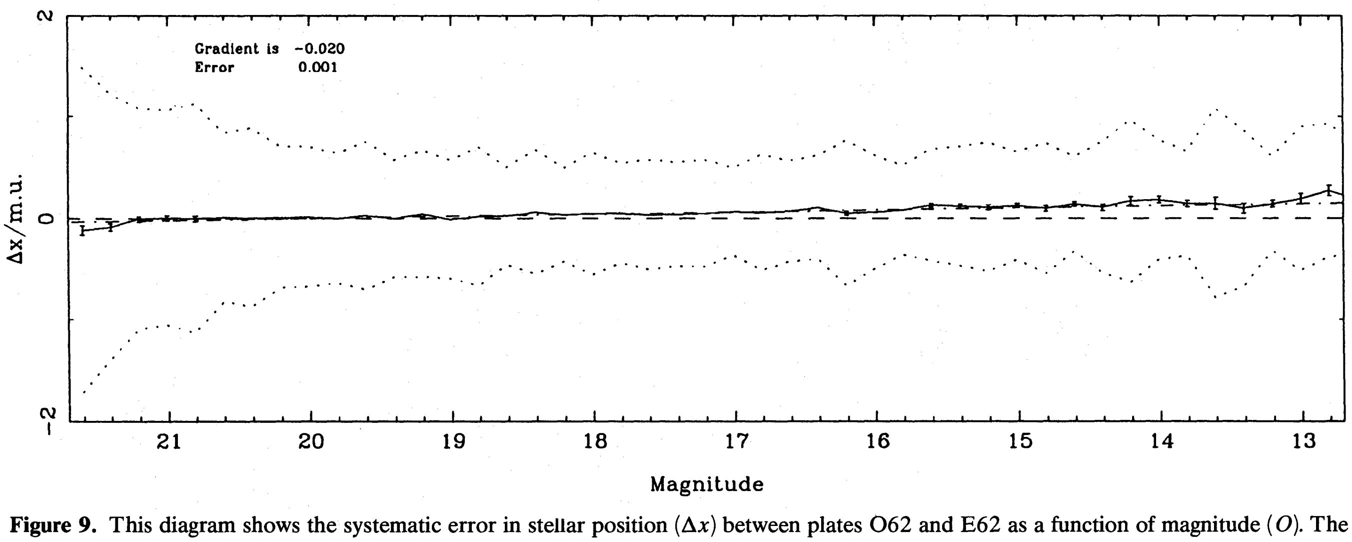

Figure 9. This diagram shows the systematic error in stellar position (Δx) between plates O62 and E62 as a function of magnitude (O). The solid line represents the average error, while the dotted line gives an indication of the spread in the errors. A best-fitting straight line has been fitted to the data (dot-dashed) and the gradient of this line (in machine units mag^{-1}) is shown.

Table 2. This table shows the measured values of the gradient of a linear fit compared to the average stellar position change (between reference and comparison plates) as a function of magnitude. The underlined plates are originals, while the others are copies. The gradient measurements are in machine units mag^{-1}, for the O/E combination the magnitude in question is O, while for the UK Schmidt plates it is a J APM magnitude, i.e. $2.5 \log_{10} I_{\mathrm{iso}}$. Therefore no direct comparison between the two data sets should be made. The measuring error in these gradients is about 0.002.

Reference Plate	Comparison Plate	g_x	g_y
O62	E62	-0.020	0.000
O1558	E1558	0.003	-0.007
O1385	E1385	-0.006	0.014
O1613	E1613	0.014	0.011
<u>J6814</u>	<u>J6644</u>	-0.020	-0.006

using UK Schmidt plates. In all these cases the plate pairs had little epoch difference, therefore any effect seen is due to a systematic measuring or recording error and is not astronomical in origin. It should be noted that all the measurements were carried out on 0°/180° averaged data.

The size of this effect is about 0.012 machine units mag^{-1} ($=0.1$ μm mag^{-1} or 0.006 arcsec mag^{-1}) and it can affect either of the x or y directions. Numerous possibilities have been suggested for the cause of this effect.

(i) The vertical misalignment error changes with each scan causing an error which is not taken out by the 0°/180° averaging. This is not the case since the gradients (g_x and g_y) are the same for 0° and 180° scans (to within the errors expected), hence this error is intrinsic to the plate and not caused by the APM.

(ii) A combination of atmospheric dispersion (see later in this section) and different magnitudes having different average colours. This dispersion effect would cause an error only in the direction of increasing altitude (usually within 30° of the y-axis) and for it to cause a shift of 0.024 arcsec between two groups of stars (21- and 17-mag stars, $g_y=0.006$ arcsec mag^{-1}, O and E plates, zenith angle $\sim 45°$), it would require a difference in $(B-V)$ of about 0.1. Although the magnitude of this difference in $(B-V)$ is within reason, the predicted direction of the error does not agree with the measured values.

(iii) A possible explanation is that the emulsion has sheared, either during processing or storage. The reason for a shear causing an error of this type is similar to the reasons for the vertical misalignment error. For an emulsion that is 25 μm thick, a shear of around 2° [$\approx \tan^{-1}(0.4\ \mu\mathrm{m} \times 2/25\ \mu\mathrm{m})$] could account for this error.

(iv) Another possibility for copied plates is that if the master plate is not held perpendicularly to the illumination source, a magnitude effect will be seen in the copied plates. Using the same arguments as in (c) the error in the illumination system must be around 2° to cause a systematic error of the magnitude seen. This argument does not explain why the error is also seen on the original plates.

(v) If there are telescope tracking errors or problems with the optics, then it is possible that the images might become asymmetrical. When this is combined with the intensity-weighted method of determining the position of an image, along with cut-offs from saturation and the isophotal limit, then a magnitude-dependent systematic error may result. This is the most likely explanation.

Since the cause of this error remains uncertain and because it seems to be random, no prediction can be made in order to remove it from the data. Neither can the 'measurement and subtraction' technique be used, since proper motions of various groups of stars are magnitude dependent, e.g. faint stars are statistically further away than bright stars, hence their proper motion due to the solar motion will be smaller. Any subtraction of magnitude-dependent terms will remove this astronomical information. Chiu (1980) also found similar terms, but was able to carry out some form of correction since he had data from several epochs.

Because no correction is possible for this error, it will provide one of the limits to the accuracy of the final measurements. Estimates show that this error could change the values measured for the solar motion, $S_{\odot}$, by ~ 0.45 km s^{-1} and the parallactic zero point by ~ 0.0005 arcsec yr^{-1}.

As with most telescopes, the image quality of a Schmidt deteriorates further away from the field centre (Linfoot 1955). However, the image only becomes asymmetrical if the corrector plate of the Schmidt is misaligned (Bowen 1960) and, arising from the effects of saturation and using an isophotal measurement of the position of a star, this will give a magnitude dependence to the error of measuring these positions. This is similar to the problem mentioned in (v) above.

This effect has been noticed in the 8- and 12-h fields as a radial error (Δr), which is a function of magnitude and radial distance from the plate centre. An example is shown in Fig. 10. This diagram shows the largest effect that has been seen, a shift of ~ 3.2 μm for 14th magnitude stars at the plate edge. It was expected that this error would be the same if the same type of comparison, i.e. the same telescope and emulsion combinations, was carried out but in a different field. This was not the case. Considering only the J, O and E plates, the errors are consistent with this systematic effect being present in the 8-h field plates only on O62 and for the 12-h field only on J7781. When any two plates are compared in these fields, not including O62 nor J7781, no effect is seen.

For the 11- and 15-h fields, the situation is complicated by the fact that the primary and secondary epoch plates do not have the same plate centres. Additionally, since these plate centres are not central with respect to the scanned regions, the errors will interfere with the measurement of the x and y errors that are a function of magnitude (and vice versa). When the radial errors for these two fields were measured (taking into account the different plate centres), all errors were found to be less than 1.2 μm for 14th-magnitude stars at the plate edge. It can be shown that a radial error of this

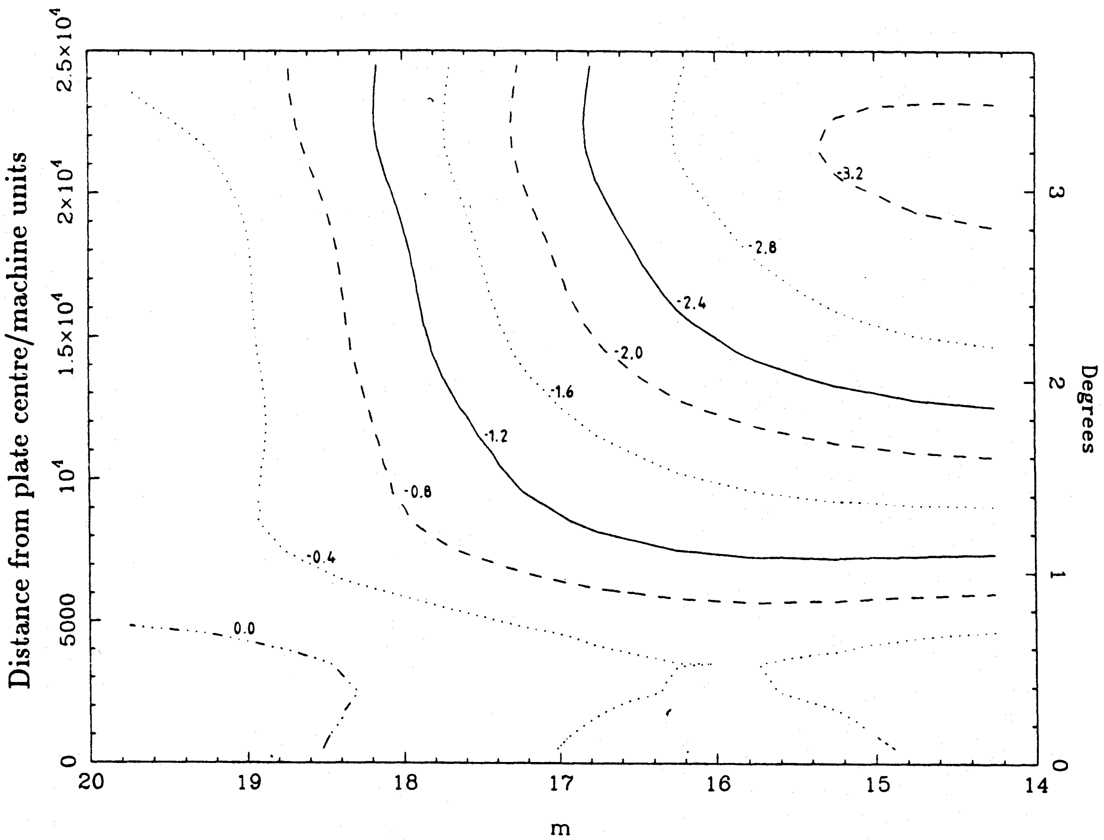

Figure 10. This diagram shows the radial error (Δr) between plates O62 and E62 as a function of radius and magnitude (O). The units of the contours are in micrometres.

Table 3. This table gives the values of ζ, B and η ($=\sec\zeta$) for all the J, O and E plates used in this project. ζ and B are in degrees.

Plate	ζ	B	η
J6814	51.3	197.8	1.60
J6644	50.1	192.4	1.56
O62	16.7	18.3	1.04
E62	21.3	39.5	1.07
J4205	11.3	176.6	1.02
O1558	56.2	-22.8	1.80
E1558	53.8	-15.5	1.69
J7781	44.2	165.8	1.39
O1385	22.7	-14.6	1.08
E1385	22.0	5.2	1.08
J5779	32.8	196.7	1.19
O1613	41.7	33.4	1.34
E1613	37.4	24.1	1.26

size will cause an average shift in x and y (averaged over the scanned region) for the 11-h field of 0.24 and 0.32 μm (respectively) and for the 15-h field −0.40 and −0.16 μm. The average shift for 14th-magnitude stars due to the magnitude-dependent errors mentioned earlier in this section is 0.64 μm. Therefore the effect of this radial error in these two fields on the measurement of $S_\odot$ and the parallactic zero point will be small and is ignored.

For the 8- and 12-h fields, even though the errors are ~ three times larger, owing to the plate centres being close to the centre of the scanned region, the effect on the average position of 14th-magnitude stars will be to shift them by ~ 0.08 μm. Again no correction is made for this error.

It should be noted that this error does not significantly affect the results of the high-proper-motion analysis in Paper I. This is due to the fact that the largest effect seen is five times smaller than the proper-motion limit used.

Radial errors as a function of colour were also investigated, but were found to be smaller (by about a factor of four) than those that were a function of magnitude, and hence were also ignored.

Another systematic error that is a function of photometry is due to atmospheric dispersion (Murray 1983, chapter 7; van de Kamp 1967). This is caused by the refraction of light through the atmosphere being a function of wavelength and images of different colour having different effective wavelengths, hence there is a shift in the direction of increasing altitude which is dependent on the colour of the image. For measuring absolute proper motions, the absolute value of

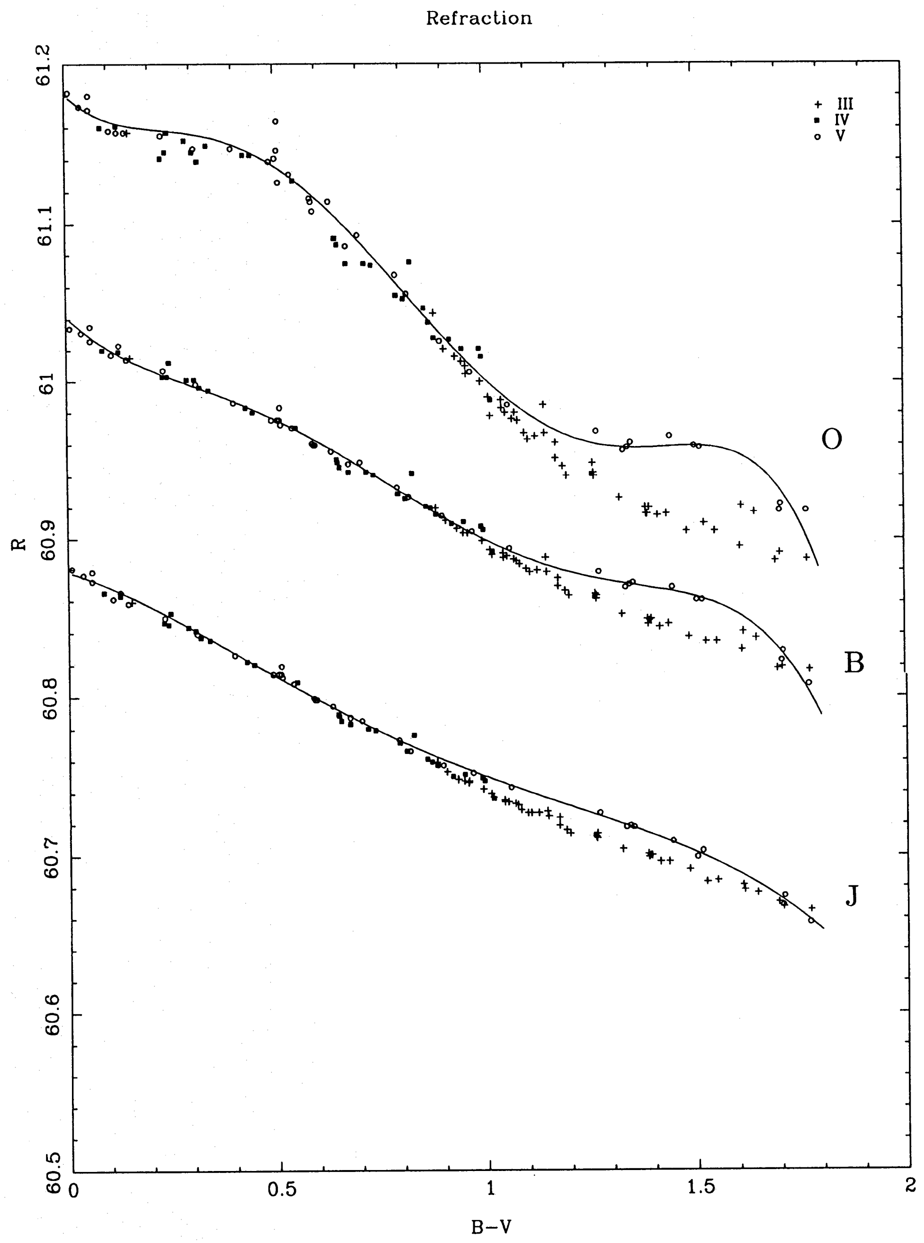

Figure 11. This diagram shows the constant of refraction, R, as a function of $(B-V)$ for the emulsion/filter responses O, B and J. The various symbols stand for different types of star. The lines drawn are best-fitting polynomials (coefficients given in Table 4) to the main-sequence stars.

refraction is not needed to high precision, since it is the difference in refraction between that for the average colour of all galaxies (which define the reference frame) and that for the colour of each star that is important.

These colour terms cannot be calculated directly from the data in the form of an additional term in the plate solution, cf. Chiu (1980), for similar reasons as those that explain why magnitude terms cannot be subtracted from the data, i.e. the proper motions of various groups of stars are colour dependent, e.g. blue stars are predominantly low-metallicity stars and have different kinematic properties to red stars (mainly thin disc).

The corrections that should be added to the proper motions to account for atmospheric dispersion are

$$\Delta\mu_\alpha \cos\delta = \{[R_s(C_{Ga}) - R_s(C_{St})] \sin B_s \tan \zeta_s - [R_p(C_{Ga}) - R_p(C_{St})] \sin B_p \tan \zeta_p\}/\Delta t, \qquad (1)$$

$$\Delta\mu_\delta = \{[R_s(C_{Ga}) - R_s(C_{St})] \cos B_s \tan \zeta_s - [R_p(C_{Ga}) - R_p(C_{St})] \cos B_p \tan \zeta_p\}/\Delta t, \qquad (2)$$

where R is the constant of refraction appropriate for images of colour C, ζ is the zenith angle for the exposure, B is the parallactic angle (direction angle to the zenith measured

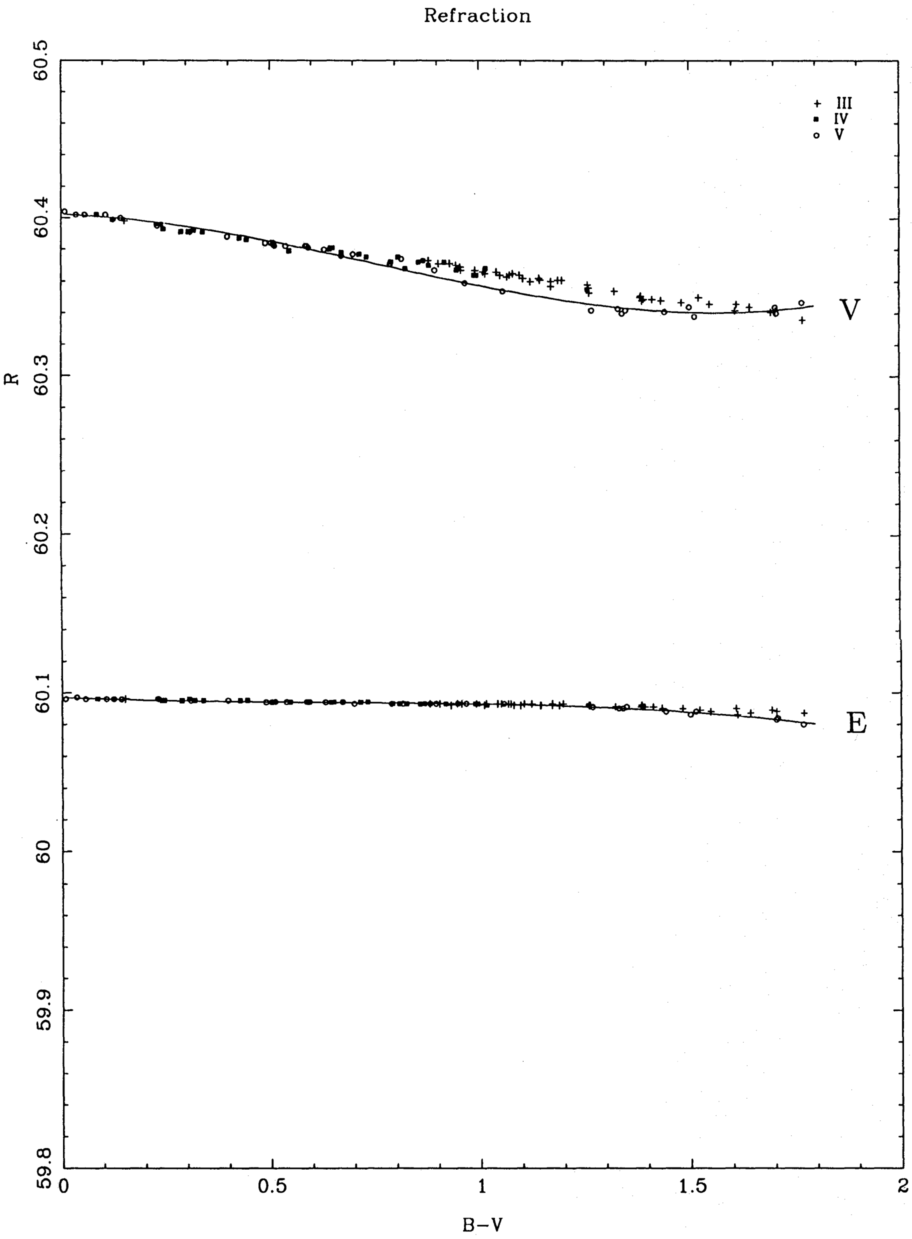

Figure 12. The same as Fig. 11 but for the emulsion/filter responses V and E.

from north and positive in the direction of increasing RA) and Δt is the epoch difference. The subscripts p and s refer to the primary and secondary epoch plates. C_{Ga} refers to the average colour of all galaxies and C_{St} refers to the colour of an individual star. The values of ζ, B and η ($=\sec\zeta$) for all the J, O and E plates used in this project are given in Table 3.

$R(C)$ is calculated using the values for $R(\lambda)$ given in Allen (1973), for 0° C, pressure 760 mm Hg and water-vapour pressure 4 mm Hg, and a relationship which was derived between colour and effective wavelength $\bar{\lambda}$. The effect of using these values rather than those for the altitude of the observatories can be calculated using relationships given in Allen (1973). It can be shown that the difference in the corrections are small in comparison with the errors in the zero-point errors.

$\bar{\lambda}$ is defined in Murray (1983) as

$$\bar{\lambda}=\frac{\int_0^\infty JD\mathrm{e}^{-\kappa\sec\zeta}\lambda\,\mathrm{d}\lambda}{\int_0^\infty JD\mathrm{e}^{-\kappa\sec\zeta}\,\mathrm{d}\lambda}, \tag{3}$$

where J is the intensity of the source, D the response of the detector, κ is the exponential atmospheric absorption coefficient (all of which are functions of λ) and ζ is the zenith angle. J was obtained for different spectral types of star from Gunn & Stryker (1983), κ from Allen (1973) and the sources for the different response functions (D) are the same as those given in Evans (1989).

Table 4. This table gives the polynomial coefficients for the relationships between refraction constant, R, and $(B-V)$ for various emulsion/filter responses. Separate relationships are given for dwarfs and giants. The polynomials are valid in the range $0.0<(B-V)<1.8$ and have been calculated with an air mass of 1. The constant of refraction (in arcsec) can then be calculated from this equation $R=\sum_n a_n(B-V)^n$.

Emulsion/ Filter	Stellar Type	a_0	a_1	a_2	a_3	a_4	a_5
O	Dwarf	61.181	-0.265	1.216	-2.5546	1.8804	-0.4554
O	Giant	61.152	0.099	-0.400	0.1492	—	—
B	Dwarf	61.042	-0.270	0.709	-1.2770	0.9210	-0.2270
B	Giant	61.027	-0.064	-0.113	0.0469	—	—
J	Dwarf	60.878	-0.083	-0.180	0.1940	-0.0597	—
J	Giant	60.882	-0.140	-0.012	0.0127	—	—
V	Dwarf	60.402	-0.010	-0.064	0.0286	—	—
V	Giant	60.404	-0.037	—	—	—	—
E	Dwarf	60.097	-0.011	0.014	-0.0074	—	—
E	Giant	60.096	-0.001	-0.002	—	—	—

Figs 11 and 12 show the constant of refraction as a function of $(B-V)$ for various responses. The lines drawn through the data points represent the best-fitting polynomials for main-sequence stars. Table 4 gives the polynomial coefficients for the best-fitting polynomials for dwarfs and giants for the five responses considered (O, B, J, V and E). In Murray & Corben (1979), a similar calculation was carried out for the emulsion/filter responses IIaO/GG385 ($\equiv$B) and IIaD/GG495 ($\equiv$V) using the Vilnius stellar spectra (Straižys & Sviderskienė 1972). There is good agreement between their fig. 4 and Figs 11 and 12 from this work to within a small constant offset (<0.15 arcsec).

It should be pointed out that all the data presented have had $\bar{\lambda}$ calculated using an air mass (η) of 1, i.e. $\zeta=0°$. To see what would be the effect of a greater air mass, the same calculation was carried out for the J response with $\eta=1.8$. In going from $(B-V)\approx0.8$ (average colour for galaxies) to $(B-V)\approx1.5$ (M dwarfs) the difference in R decreased by only 0.004 arcsec in going from $\eta=1$ to $\eta=1.8$. Since the effect of air mass is much smaller than the other errors involved in calculating the correction due to atmospheric dispersion, $\eta=1$ is used in all the calculations.

For typical red stars (MO), $(O-E)=2.7$, the corrections for the different fields are in the range 1–2 mas yr^{-1}.

In order to find out how well these relationships can predict this colour term, the difference in stellar position between the O and E plates (no possible astronomical effect) for each field was plotted as a function of colour $(O-E)$. Only the faintest two magnitudes are used in these plots so as to minimize any interference from the magnitude-dependent errors. Fig. 13 shows the Δy plots for the four fields. Superimposed on these plots are the predicted shifts. Only the main sequence relationships have been used for these predictions. As can be seen, the predictions agree quite well with the measurements. It is only in the y-direction of the 15-h field that any significant departure from the prediction is seen. This shift of $\sim1\ \mu$m could be present on either plate and might cause a shift in the parallactic zero point of ~0.002 arcsec yr^{-1}. Therefore, caution should be used if this data point is used in determining Oort's constants.

The biggest source of error in carrying out these predictions is the accuracy of the average galaxy colour. Due to the uncertain nature of galaxy photometry an error of 0.1 mag in the average colour can be expected. This will cause an error in the refraction constant used, of ~0.005 arcsec, and assuming a baseline of 25 yr will give a parallactic zero-point error of 0.2 mas yr^{-1}.

Owing to the non-linearities of the photographic emulsion, it is expected that these corrections should be a slight function of magnitude. This effect was first noticed by Bergstrand (1905). Using the O and E data, an attempt to measure this effect was made. Since no effect was observed, this is not an important systematic error in this project.

6 ACCURACY

6.1 Random errors

The positional accuracy of the APM scanner can be estimated by comparing two different scans of the same plate and measuring the half-width (sigma of a Gaussian profile) of the distribution of the position changes. This will give the

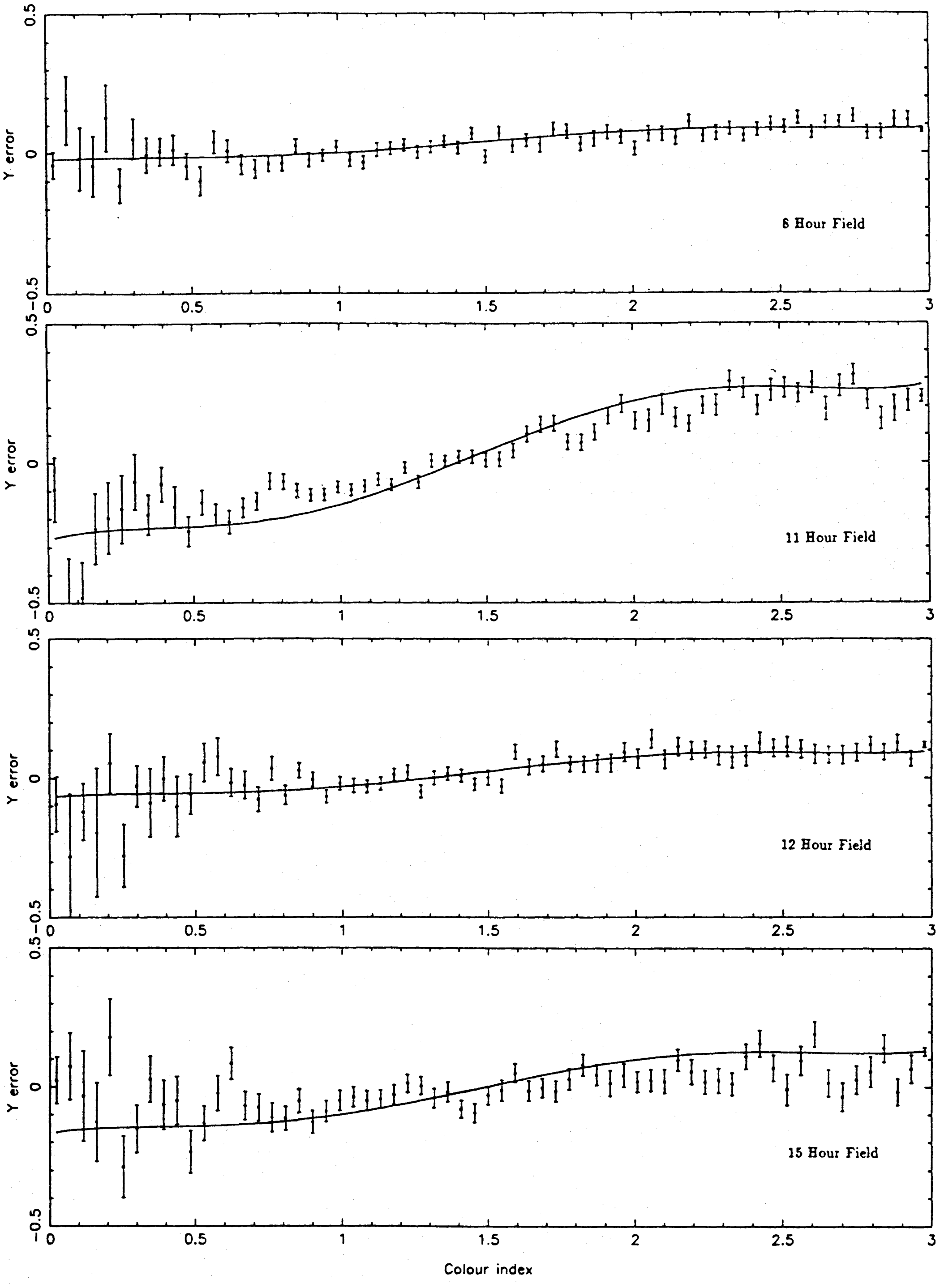

Figure 13. This diagram shows the systematic error in position (Δy) as a function of colour ($O-E$) for all four fields in the project. The units of Δy are in APM pixels which are approximately equal to 0.5 arcsec. The solid line is a prediction of the error. Only the faintest two magnitudes have been used in these plots.

contribution to the proper-motion error due to the scanning of the plates. Note that this will be $\sqrt{2}$ times as large as the error from a single scan since this is a relative positional measurement. When this measurement is carried out, the half-width of the distribution is 0.7 μm in the x-direction (0.05 arcsec for a Schmidt plate) and 1.2 μm in the y-direction. For galaxies the distributions are up to about 50 per cent larger. The difference in the size of the error for the x and y directions is caused by the dynamic focusing unit of the APM. Errors within this will contribute an additional random error (rms ~ 1 μm) to the y measurements. There is some variation in these values from plate to plate, but in general values are within 10 per cent of these quoted values.

The following values refer to only the x-direction. When two IIIaJ plates of the same region of sky taken at the UK Schmidt telescope are compared the half-width of the stellar positional error distribution is 1.4 μm. Assuming that the random errors due to the APM scanner and the plate add in quadrature, the random error contribution of IIIaJ plates to proper-motion measurement is 1.2 μm. This is similar in magnitude to intrinsic plate errors found by others, e.g. Fresneau (1978) and Chiu (1977). Similarly, comparing two POSS copy plates (103-a emulsions) a half-width of 2.3 μm is found, which yields a plate contribution to the proper-motion measurement of 2.2 μm. It should be noted here that in the last two cases the measurement errors for galaxies were about twice that of stars. The larger errors for galaxies can be understood by inspecting the equation for the minimum errors possible,

$$\mathrm{var}\,(x_0)=\frac{\sigma_G^2}{2I_t}\,\frac{4\pi\sigma_G^2\sigma_{\mathrm{noise}}^2}{I_t}, \qquad (4)$$

[cf. equation 32 of Irwin (1985)], where I_t is the total intensity, σ_{noise} is the random noise per pixel (in the same units as I_t) and σ_G is the radius at which the Gaussian profile is at e^{-1} of its peak height. This equation is strictly only applicable for faint Gaussian images, but for the majority of star and galaxy images, this is an adequate approximation. The important point to note is that the error in measuring x_0 scales as σ_G^2, and that σ_G is larger for galaxies than for stars.

An estimate can now be made for the error in measuring a proper motion using a IIIaJ plate for one epoch and a POSS copy plate for the other. Assuming addition in quadrature, the error should be 1.9 μm. This corresponds to an error of 0.005 arcsec yr^{-1} for a baseline of 25 yr. The real proper-motion distributions for a pair of plates with a 30-yr baseline will have a typical half-width of about 4 μm. The reason for the difference is that the random and systematic velocity distribution of the stars is adding to the width of the proper-motion distribution.

It should be noted that there is a slight magnitude dependence to these estimates of error. The errors quoted refer in general to stars brighter than $O=20$ mag. In this magnitude range the errors are roughly constant. This is due to the errors for the brighter objects being dominated by a combination of the measuring process and the effects of saturation and these errors are approximately independent of magnitude. Fainter than this, down to $O=21.5$ mag, the faintest objects in the project, the errors increase by factors of 2 to 3, depending on the field. For these objects, the errors are dominated by the signal-to-noise ratio of the recording medium and, as seen from equation 4, the limiting error is proportional to $1/I_t$. Therefore, great care must be taken when analysing the astronomical content of the proper-motion distribution as a function of magnitude at the faint end.

6.2 Systematic errors

The following list gives the main systematic effects along with the errors in the results that they cause.

(i) Distance-scale errors: the expected error in the photometric zero point for each plate is 0.05 mag, implying a probable colour zero-point error of 0.07. For $(O\text{-}E)$ data this implies a photometric parallax scale error for each field of about 25 per cent.

(ii) Velocity errors: since the effects of the magnitude-dependent errors are different for each coordinate (owing to these errors being different for the x and y directions on a plate) they have to be treated differently from the distance scale errors. The value of these errors is around 0.1 μm mag^{-1} in each coordinate and, for each plate-pair combination, can be taken as a random error. The difference in average magnitude between the maximum and minimum parallax bin is around 1.5 mag. This causes a systematic error in the measured gradient of the π versus μ plot which leads to errors of ~ 0.45 km s^{-1} in the velocity determination.

(iii) Zero-point errors: these errors are all in terms of mas yr^{-1}.

(a) Astrometric colour term errors: the error in the measured average galaxy colour is estimated to be $\sigma_{\overline{(O-E)}}=0.1$. Errors in the photometric zero point will affect stars and galaxies similarly and are therefore not important. The error in average star colour will be much smaller than that for galaxies. This just reflects the difference in image structure between stars and galaxies. It is possible that systematic errors in the calculation of these colour terms could lead to an effective doubling of the galaxy colour error. Since this is not the largest of the zero-point errors, its effect on the overall error is small. From the zenith angles at the time of exposure for each plate (Table 3) and a galaxy colour error of 0.1 the zero-point errors for each field due to this error are

8 hour	11 hour	12 hour	15 hour
0.34	0.10	0.24	0.20.

(b) Error in the misclassification correction: arising from counting errors in table 2.1 of Evans (1988), there is an error of 10 per cent in the correction that has been applied to the data to account for the effect of errors in classifying stars and galaxies on the proper-motion zero points. For each field this error contributes the following to the proper-motion zero-point error (the averages for the x and y directions were used),

8 hour	11 hour	12 hour	15 hour
0.07	0.08	0.13	0.07.

(c) Intrinsic errors: in determining the proper-motion zero point from the galaxies, there will be an intrinsic error which is equal to the error of measuring the proper motion of a galaxy divided by the square root of the number of galaxies used. For each field this is

8 hour	11 hour	12 hour	15 hour
0.09	0.19	0.08	0.19.

(d) Magnitude-dependent errors: this is the largest contribution to the zero-point error. This is due to the average magnitude of the stars in each parallax bin being ~ 2 mag above the faintest stars. Assuming that galaxies are affected as much as the faintest stars and taking this error to be 0.1 μm mag^{-1} in each coordinate [see item (b) above] the error for each field is

8 hour	11 hour	12 hour	15 hour
0.42	0.58	0.48	0.56.

(e) Total: the total zero-point error, calculated from a quadrature sum of the above four items, is

8 hour	11 hour	12 hour	15 hour
0.55	0.62	0.56	0.63.

6.3 Reliability of these error estimates

A very simple way of checking these estimates is to measure the proper-motion dispersion of known quasi-stellar objects (QSOs). QSOs have stellar-like images and, since they are extragalactic, have negligible proper motions. Thus their measured proper-motion dispersion will be a good measure of the stellar proper-motion error dispersion.

The Hewitt & Burbidge (1987) QSO catalogue was consulted and 42 QSOs were found in the 8-h field and 9 in the 12-h field. No QSOs from this catalogue were found in the 11- and 15-h fields. This uneven distribution is undoubtedly due to observer bias. The magnitude range of these QSOs was $17 \lesssim O \lesssim 20$ mag. The mean and dispersion for the proper-motion distributions of these objects are given in Table 5. These results are consistent with a properly determined absolute proper-motion zero point and proper-motion errors as estimated.

7 REDUCED PROPER MOTIONS

As described in detail in Paper I, reduced proper motions, in conjunction with a colour, are very effective in discriminating between various populations and luminosity types. A good example of this is Chiu (1980). Reduced proper motion is defined by

$$H = m + 5\log_{10}\mu + 5$$
$$= M + 5\log_{10} T - 3.379, \qquad (5)$$

where m is the apparent magnitude, μ is the total proper motion (measured in arcsec yr^{-1}), M is the absolute magnitude and T is the transverse velocity (measured in km s^{-1}).

Since it is the logarithm of the proper motion that is used in a reduced proper motion, H, it is the relative error in proper motion along with the photometric magnitude error that determines the error in H. With the high-proper-motion (HPM) sample the errors were always less than ~ 10 per cent, giving an error in H of less than ~ 0.2 mag. For the lower-proper-motion (LPM) sample a typical total proper motion is 0.010 arcsec yr^{-1}. With errors of ~ 50 per cent this leads to RPM errors of roughly 1 mag, comparable to the width of the RPM distributions. Chiu (1980), although using no proper-motion limit, had the advantage that the proper-motion errors were ~ 10 times smaller (due to the use of 4-m telescope plates and ~ 20 plates field^{-1}). Another point about the work of Chiu was that discrete classification, i.e. classifying particular stars as halo stars, for example, was not required and the results were calculated from statistical classifications which were not affected by overlapping RPM distributions.

Since the relative proper-motion errors are so large in this case it is important to calculate the effects of these errors fully. The details of this calculation is given in Evans (1988). Fig. 14 shows the RPM diagram for all stars in the 8-h field along with the predicted ridge lines (the medians of the H_0 distributions) and the widths (10 and 90 per cent points) of the predicted distributions. The populations considered and the parameters used were the same as in Paper I.

The most noticeable feature of this diagram is the way in which the increased relative proper-motion errors, along with the lack of proper-motion limits, has broadened the RPM distributions in comparison to those of the HPM sample, see figs 6 to 9 of Paper I. While there is hardly any overlap (for comparison, defined here by the 10 and 90 per cent points) of the RPM distributions with the HPM sample, within the LPM sample the overlaps are as large as 1.5 mag, which are comparable to the widths of the distributions.

Table 5. This table gives the mean and dispersion for the proper motion distributions of the QSOs in the 8- and 12-h fields.

		$\langle\mu\rangle$	σ
8 Hour Field	α	**0.6 ± 0.7**	**5.0 ± 0.6**
	δ	**0.0 ± 0.7**	**4.8 ± 0.5**
12 Hour Field	α	**1.6 ± 1.3**	**3.8 ± 1.0**
	δ	**−1.5 ± 1.3**	**3.8 ± 1.0**

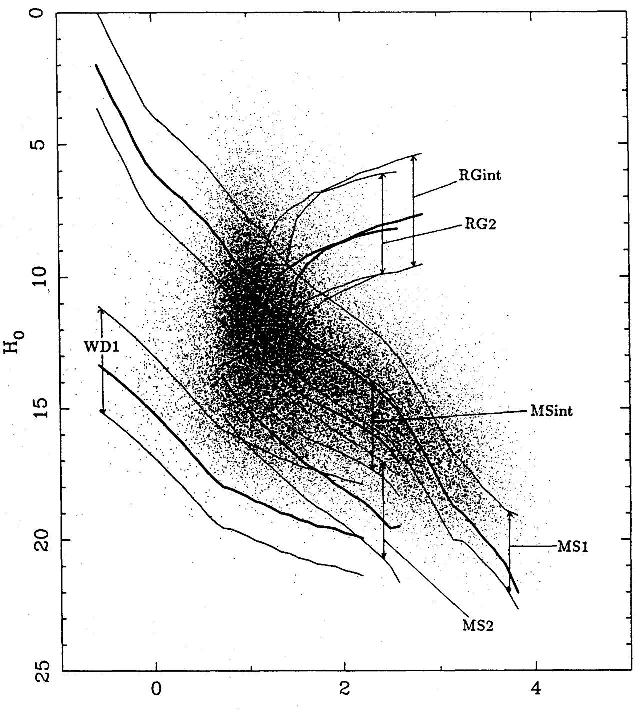

Figure 14. This diagram shows a scatterplot of colour $(O-E)$ versus reduced proper motion, $H_0 = O + 5\log_{10}\mu + 5$, for all stars in the 8-h field. The predicted medians (thick lines) of the H_0 distributions for six different populations have been drawn. These are the main-sequence stars of the thin disc (MS1), thick disc (MSint), and spheroid (MS2), red giants and subgiants of the thick disc (RGint) and spheroid (RG2) and white dwarfs of the thin disc (WD1). Either side of the ridge lines have been drawn for the 10 and 90 per cent limits of these distributions.

Therefore it is not possible to make classifications of high probability as was possible with the HPM sample.

To extract any useful information from such diagrams would require a full kinematic model and is beyond the scope of this current project. It is quite likely that the results that would be obtained from such work would be ambiguous to interpret owing to many of the parameters being strongly dependent on each other.

8 SOLAR MOTION AND DIFFERENTIAL KINEMATICS

8.1 Galactic model

The two main systematic motions that can be detected in proper-motion data are due to solar motion and differential Galactic rotation. The first causes the measured proper motion to increase linearly with parallax π while the effect of the second is a constant zero-point shift in proper motion.

The method used to calculate the solar motion is the same as that used in Paper I, i.e. Airy's method. Since this sample does not have a proper-motion limit it is possible to measure both the magnitude and direction of the solar motion, unlike the HPM sample. For the ith region the proper motions due to the solar motion as a function of parallax are given by

$$\mu_{li} \cos b_i = \frac{U\pi}{C} \sin l_i - \frac{V\pi}{C} \cos l_i \tag{6}$$

$$\mu_{bi} = \frac{U\pi}{C} \cos l_i \sin b_i + \frac{V\pi}{C} \sin l_i \sin b_i - \frac{W\pi}{C} \cos b_i \tag{7}$$

where μ_{li} and μ_{bi} are the proper motions in the directions of increasing Galactic longitude and latitude (both measured in arcsec yr^{-1}) (l_i, b_i) are the Galactic coordinates of the region, (U, V, W) are the components of the solar velocity in the Galactic triad in $\mathrm{km\,s^{-1}}$ and $C = 4.74$.

It should also be noted that these equations do not have any terms due to differential Galactic rotation and therefore to calculate the solar velocity it is the gradient of the proper motion versus parallax plots for each region that is used. Again, the method of least squares is used to derive values for (U, V, W) in a manner similar to that used for the HPM sample.

The early work on the observational effects of the rotation of the Galaxy was carried out mainly by Lindblad and Oort. In Lindblad (1925), and other papers of his, a hypothesis was suggested in which the Galaxy was divided into subsystems which rotated about a common axis. The majority of stars in the local neighbourhood, including the Sun, formed one subsystem which rotated about the Galactic centre with a local neighbourhood velocity of $\sim 300\ \mathrm{km\,s^{-1}}$. RR Lyrae variables and globular clusters formed another subsystem which had a very low rotation velocity. This simple hypothesis would explain the systematic motions observed for this second group of objects. Oort (1927a) confirmed the rotation of the Galaxy by studying the variation of radial velocities as a function of Galactic longitude. In this paper he introduced the Oort constants, A and B, and simple formulae for describing the observed consequences of Galactic rotation. He also measured a value for A. In Oort (1927b) he refined the measurement of A using radial velocities and using this measurement, along with proper-motion data, measured B. It should be noted that a rotation in the plane of the Galaxy had been used previously by several authors to explain systematic trends in proper motion data. Struve (1887) incorporated such a rotation term when calculating the constant of precession and Charlier (1913) measured this rotation when investigating proper motions of 4th- and 5th-magnitude stars. The investigation by Charlier is probably the first significant measurement of the constant B. This simple model was expanded by Milne (1935) to include differential expansion terms and by Murray (1986) to include a perpendicular velocity shear. This last term is needed to explain the systematic shift in the proper motions measured in Murray's analysis of South Galactic Pole (SGP) data. At the poles the simple model predicts no offset in the proper-motion measurements since all the equations contain $\cos b$ terms. To account for the measured shift a linear shear of the disc, in the direction opposite to Galactic rotation, was introduced.

Since one of the fields in this project (12 h) is close to the North Galactic Pole, the Murray shear is included in the following analysis. A detection of this shear in this field would provide an independent confirmation that this effect is applicable to the Galaxy as a whole and not to one isolated area, the SGP.

The differential expansion terms C and D (Murray 1983) are, however, not included. This is for two reasons: (a) with four fields there are effectively only eight proper-motion offsets; calculating five parameters from these data points would probably not produce a reliable result and (b) for the sample of stars considered, the differential expansion terms will be small (Balona & Feast 1974).

After the effects of the Solar motion have been removed from the proper-motion data, the remaining motions are due to the effects of differential rotation of the Galaxy. To calculate these motions, the velocity of the group of stars in question relative to the local mean velocity, v_0, is required. The velocity of this group of stars in the Galactic triad is given by $v_s = \omega R(\sin\phi, \cos\phi, 0)$ and the local mean velocity by $v_0 = \omega_0 R_0(0, 1, 0)$, where ω is angular velocity and R is the projected distance to the Galactic centre. R_0 is taken to be 8.5 kpc as recommended by Kerr & Lynden-Bell (1986). Fig. 15 illustrates this and shows how ϕ is defined.

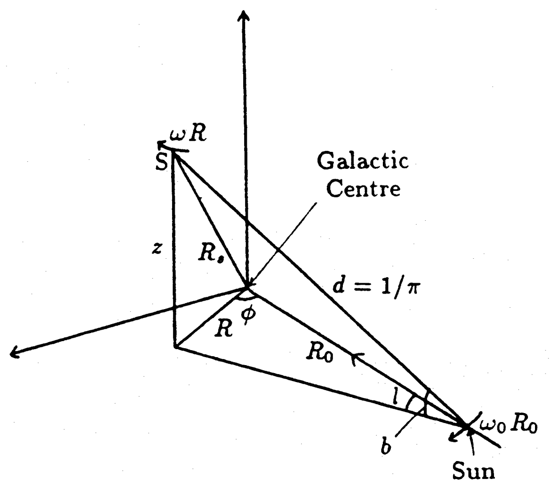

Figure 15. Diagram illustrating quantities defined in text.

Therefore the relative velocity is given by

$$v_{\rm rel} = v_s - v_0 = (\omega R \sin\phi, \omega R \cos\phi - \omega_0 R_0, 0). \tag{8}$$

From the definitions of A, B and M,

$$A = -\frac{R_0}{2}\left(\frac{\mathrm{d}\omega}{\mathrm{d}R}\right)_{R=R_0},$$

$$B = -\omega_0 - \frac{R_0}{2}\left(\frac{\mathrm{d}\omega}{\mathrm{d}R}\right)_{R=R_0},$$

$$M = R\left(\frac{\mathrm{d}\omega}{\mathrm{d}|z|}\right)_{z=0}, \tag{9}$$

and assuming that the velocity field is linear, a relation for ω is obtained:

$$\omega = A - B + \frac{2A}{R_0}(R_0 - R) + \frac{|z|M}{R}. \tag{10}$$

To obtain the proper motions (in arcsec yr^{-1}), μ_l and μ_b, in the directions of increasing Galactic longitude and latitude, the scalar product of $v_{\rm rel}$ is formed with two of the unit vectors of the Galactic normal triad, $\tilde{p}_{\rm G}$ and $\tilde{q}_{\rm G}$ (Murray 1983), and this is then multiplied by the parallax. Therefore

$$\begin{aligned}\mu_l \cos b &= (\tilde{p}_{\rm G}\cdot v_{\rm rel})\,\pi \\ &= -A\left[\left(1+\frac{2(R_0-R)}{R_0}\right)\cos b - 2(R_0-R)\,\pi\cos l\right] \\ &\quad + B\cos b \\ &\quad + M\sin|b|\left(\frac{R_0}{R}\cos l - \frac{1}{\pi R}\cos b\right).\end{aligned} \tag{11}$$

In Oort's analysis a further geometric approximation was made, i.e. that $R_0 - R \approx d\cos b\cos l$. Using this and ignoring any terms with $(\pi R_0)^{-1}$ we obtain

$$\mu_l \cos b \approx (A\cos 2l + B)\cos b + M\sin|b|\cos l, \tag{12}$$

of which, the first part is the well-known Oort formula. Similarly,

$$\begin{aligned}\mu_b &= (\tilde{q}_{\rm G}\cdot v_{\rm rel})\,\pi \\ &= -2A(R_0-R)\,\pi\sin b\sin l - M\frac{R_0}{R}\sin|b|\sin b\sin l \qquad (13) \\ &\approx -\frac{1}{2}A\sin 2l\sin 2b - M\sin|b|\sin b\sin l. \qquad (14)\end{aligned}$$

For some fields, the Oort geometric approximation breaks down quite rapidly, e.g. for the 11- and 12-h fields at a distance of 1 kpc, this approximation is wrong by a factor of ~2. Therefore equations (11) and (13) were the ones used in the analysis. A, B and M were calculated from the data using these equations and the method of least squares.

A note about the units of the quantities in these equations. Given that R_0, R and π^{-1} are all in the same units, the units of A, B and M will be the same as those of the proper motions, i.e. arcsec yr^{-1}. To convert into the more familiar units of km s^{-1} kpc^{-1} these quantities must be multiplied by 4740.

The proper motions in this analysis were calculated by simply dividing the change in position of the star (the average for the 0° and 180° scans) between the primary- and secondary-epoch plates by the time difference between the two epochs. The average proper motion for a parallax bin was calculated from the mean of the distribution after removing stars with proper motions greater than 3σ away from the centre of the distribution. The 3σ limits were estimated using a procedure similar to quartile estimation. This method was adopted since it was more robust than a straightforward calculation of the mean.

8.2 Distance estimates

The parallax of each star was calculated using the $(O-E)$ photometry, a colour–magnitude relation and allowance for extinction as given in Table 1. $(E-I)$ photometry could not be used since no I plate was available in the 11-h field and using only three fields would severely reduce the reliability of the astrometric result. The stars were also restricted to a central 2°-radius area so that systematic errors from photometric field effects would be kept to a minimum.

The main sample of stars used in this analysis had $(O-E)>2.0$ (approximately redder than K5) and were in the parallax range $0.001<\pi<0.005$ arcsec $(200<d<1000$ pc). In this colour range, the contamination by giants would be negligible and the parallax range restricted the stars to mainly those of the thin disc. Assuming a 300-pc scaleheight thin disc and a 1000-pc, 2 per cent local normalization thick disc, at a height of 1 kpc, the fraction of thick-disc stars present was ~20 per cent. The effects of possible thick-disc contamination is discussed later on. A similar investigation using bluer stars was also carried out, but in this case the contamination by various populations is far more severe. This is discussed after the results for the red star sample.

As the preliminary results were being investigated, it became apparent that the distance scale was systematically in error. The parallaxes were calculated from the $(O-E)$ data, transformed to $(B-V)$ using relations given in Evans (1989) and an absolute magnitude calculated using the colour–magnitude relation given in Chiu (1980). A further transformation, $(O-E)$ to $(O-V)$, enabled a V apparent magnitude to be calculated and thus a photometric parallax. Numerous possible explanations were investigated, but comparison of these photometric relations with photoelectric photometry of very red stars in Thé, Steenman & Alcaino (1984) showed that they were in error by ~0.1 for stars redder than $(O-E)\sim 2.5$ $((B-V)\sim 1.4)$.

Since the passbands were the same as those used by Bessell (1986), where the relations were derived from the Vilnius spectral atlas, it is concluded that the spectra for the reddest ~10 dwarfs in Gunn & Stryker (1983) are unreliable to some extent. In this paper it does state that these spectra were intended to synthesize galaxy spectra and 'may or may not suffice for other purposes'. A systematic correction to the fluxes in Gunn & Stryker is suggested by Rufener & Nicolet (1988), but these are far too small to account for the systematic errors found here.

Although this error is small and does not significantly affect the star-count comparisons carried out in Evans

(1988) nor the predicted RPM distributions, it does have a significant effect on photometric parallaxes calculated from $(O-E)$ data. The $(E-I)$ to $(R-I)$ transforms can, however, be regarded as being quite reliable. One of the reasons for this is that the relationship is close to being linear with a gradient of one and that the passbands are comparable. This means that any errors in the spectra which affect the E passband will affect the R passband in a similar manner and the derived transformation will be very close to the true one. Also, as pointed out in Gunn & Stryker (1983), it is probably the blue region of the spectra for red stars that is in error and therefore the red passbands should be affected to a lesser degree than the O and B passbands. It should be noted that the derived transformations for stars bluer than $(B-V)=1.4$ are not affected, as is seen in the comparisons with the photometry of Menzies, Banfield & Laing (1980) (see fig. 12 of Evans 1989).

To provide a better distance scale a transformation between $(O-E)$ and $(E-I)$ was derived directly from the photographic data in the 8- and 12-h fields. The 15-h field data was considered possibly to be inaccurate, owing to the low value of scaleheight derived from it in the star counts analysis in Evans (1988). The results are given in Table 6. This relationship enables the $(O-E)$ data to be used in conjunction with the $(E-I)$ transforms to calculate photometric parallaxes.

In Evans (1988) it was pointed out that due to the presence of random errors in the photometric data, there would be a systematic bias present in any derived distance. Similarly, random errors in the photometry cause systematic biases in the photometric parallax measurements. In a procedure similar to that of Evans (1988) it is found that the expected value for the true parallax is given by

$$\langle\pi_t\rangle = \frac{\displaystyle\int_0^\infty \pi_t^{-2}\exp[-(1/\pi_t\beta)]\exp\left[-25\left(\log_{10}\frac{\pi_0}{\pi_t}\right)^2\Big/2\sigma^2\right]\mathrm{d}\pi_t}{\displaystyle\int_0^\infty \pi_t^{-3}\exp[-(1/\pi_t\beta)]\exp\left[-25\left(\log_{10}\frac{\pi_0}{\pi_t}\right)^2\Big/2\sigma^2\right]\mathrm{d}\pi_t} \tag{15}$$

where σ is the error in distance modulus, β is the scale distance of an exponential density law and π_t and π_0 are the true and observed parallaxes respectively. The magnitude of the distance modulus errors is $\sigma=0.88$. In the parallax range considered, this bias affects the parallaxes by between $+20$ and -10 per cent. The effect of not using these bias corrections on the overall results is to reduce the solar motion by ~ 15 per cent and to change the A and B Oort constants by ~ 2 km s^{-1} kpc^{-1}. The change in the Murray velocity shear, M, was larger, ~ 7 km s^{-1} kpc^{-1}.

Table 6. This table shows the relationship between $(O-E)$ and $(E-I)$ derived directly from the photographic data in the 8- and 12-h fields.

(O−E)	2.00	2.10	2.20	2.30	2.40	2.50	2.60	2.70	2.80	2.90	3.00	3.10	3.20
(E−I)	0.55	0.58	0.62	0.65	0.67	0.73	0.80	0.88	1.05	1.19	1.29	1.43	1.61

8.3 Results

The random errors on the proper-motion measurements for each parallax bin are quite small, of order 1 mas yr^{-1} or less. These are simply calculated by dividing the half-width (sigma of a Gaussian distribution) by the square root of the number of stars in the bin. The systematic errors are, however, more serious and have a large effect on the proper-motion zero points and hence the measurement of the Oort constants. Since each of the errors (detailed in Section 6) contributes to the final errors of the measured parameters in a different way, the overall errors have been computed using a Monte Carlo method.

The results of this analysis for the main sample of stars are given in Table 7 and the proper-motion versus parallax plots for the four fields are shown in Figs 16 and 17. The error bars shown in these diagrams do not show the systematic errors and show only the random measuring errors. Note that the systematic errors are about 0.6 mas yr^{-1} for each coordinate in each field.

The value of the Solar velocity derived for this sample of stars is in reasonable agreement with that of the basic solar motion (9, 11, 6) km s^{-1}, and the position of the solar apex from the thin-disc subset of the HPM sample in Paper I. Fig. 18 shows the position of the solar apex derived here along with other determinations and various 'standard' apices. The average value for stars of spectral type K5 or redder from Wehlau (1957) (note that this is the original source for the values quoted in Mihalas & Binney 1981, and Delhaye 1965) is (8.5, 18.8, 7.1) km s^{-1}, again in reasonable agreement with the values derived in this project. It should be noted that the solar velocity derived in these sources varies quite considerably (by up to 7 km s^{-1}) as a function of spectral type. Using data for nearby (within 20 pc) stars, Jahreiß & Wielen (1983) calculated the Solar velocity with respect to various groups of stars. For K5, and redder, stars the average solar velocity was found to be (8, 28, 11) km s^{-1}. Although the apex for this velocity is similar to that of this project and that of Wehlau, the magnitude is ~ 50 per cent bigger. It is unclear why this determination is significantly different and why there is so much variation of the solar velocity as a function of spectral type.

A recent determination of the solar apex by Hanson (1987a) using data from the Lick Northern Proper Motion Program, a project similar to this one, is probably not directly comparable because the sample of stars he used was contaminated by a large number of non-thin disc stars. The subsample of these stars which is probably least contaminated is that with $0°<|b|<20°$. The position of the solar apex determination for these stars is shown in Fig. 18 and is again reasonably close to this project's value.

The values derived for the Oort constants A and B are consistent with the most recent determinations, but owing to the large errors it is not possible, with this data, to discriminate between other peoples' results. The value for the velocity shear in the z-direction of $M=-21\pm7$ km s^{-1} kpc^{-1} is in moderate agreement with that found originally by Murray (1986) in the southern Galactic hemisphere of $M=-36\pm5$ km s^{-1} kpc^{-1}. The validity of this additional term to the Lindblad–Oort model can be seen in the 12-h field μ_b versus π plot in Fig. 17. If no M shear had been used, the derived values for A and B would have been 20 and -11 km s^{-1}

Table 7. This table shows the results of the kinematical analysis of stars with $(O-E)>2.0$ and $0.001<\pi<0.005$ arcsec from the four fields of this project. (U, V, W) is the solar velocity, in Galactic coordinates, with respect to these stars, (l, b) is the corresponding position of the Solar apex and A, B and M are the differential Galactic rotation parameters.

U	7.3 ± 1.5 km/s
V	13.9 ± 2.3 km/s
W	8.8 ± 2.2 km/s
l	62 ± 6 °
b	29 ± 7 °
A	19 ± 6 km/s/kpc
B	-13 ± 5 km/s/kpc
M	-21 ± 7 km/s/kpc

kpc^{-1} respectively, indicating a relationship shown as the dashed line. This is offset by about 5 mas yr^{-1} from the data points and cannot be accounted for by known systematic errors in the data and probably indicates that the model used (without M) is inadequate. This is contrary to the conclusion of Reid (1990) where no strong evidence for a vertical shear of this magnitude was found. However, other determinations have been made of this shear by Hanson (1987b) (-30 km s^{-1} kpc^{-1}) and Soubiran (1993) (-40 km s^{-1} kpc^{-1}) in the northern Galactic hemisphere and by Guo et al. (1993) (-35 km s^{-1} kpc^{-1}) in the south. As can be seen, the value found in this project is lower than the other determinations. Looking more closely at the 12-h field plot of Fig. 17 it can be seen that in this field of high Galactic latitude, the best-fitting model has a smaller offset than the data points. It seems likely that the simple model used for the variation of the shear as a function of Galactic coordinates needs some alteration.

There are also other offsets present of ~2 mas yr^{-1}, significantly larger than the expected errors in the proper-motion zero points of ~0.6 mas yr^{-1}. Further elaboration of the kinematic model using this data would be inadvisable due to there being only four fields in the project.

In a recent review of the Galactic constants (Kerr & Lynden-Bell 1986) the mean values for the Oort constants

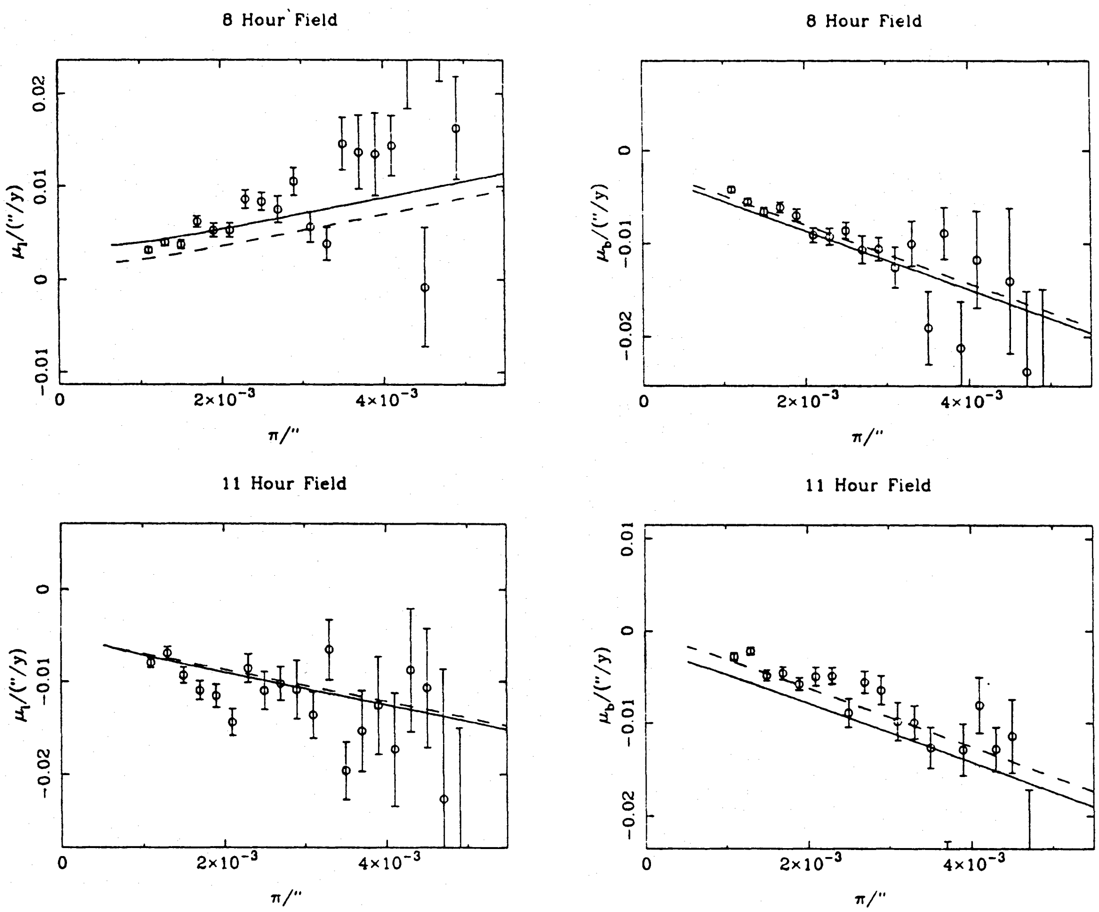

Figure 16. These diagrams show the proper motion versus parallax plots for the 8- and 11-hour fields. The stars considered in this analysis had $(O-E)>2.0$, $0.001<\pi<0.005$ arcsec and were in a central 2°-radius area of the field. The solid line is the Lindblad–Oort model plus the velocity shear in the z-direction, and the dashed line is the same model without this shear. The error bars just represent the random measuring errors.

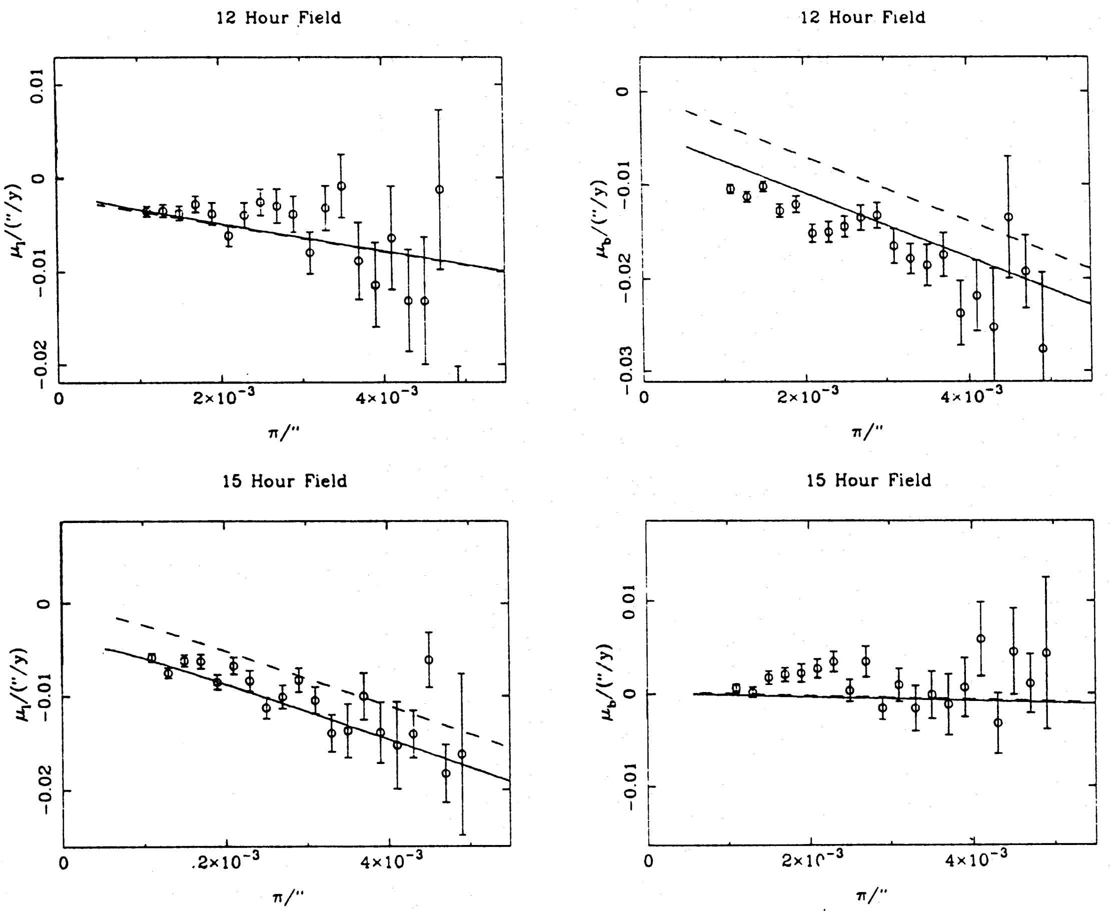

Figure 17. The same as Fig. 16 but for the 12- and 15-h fields.

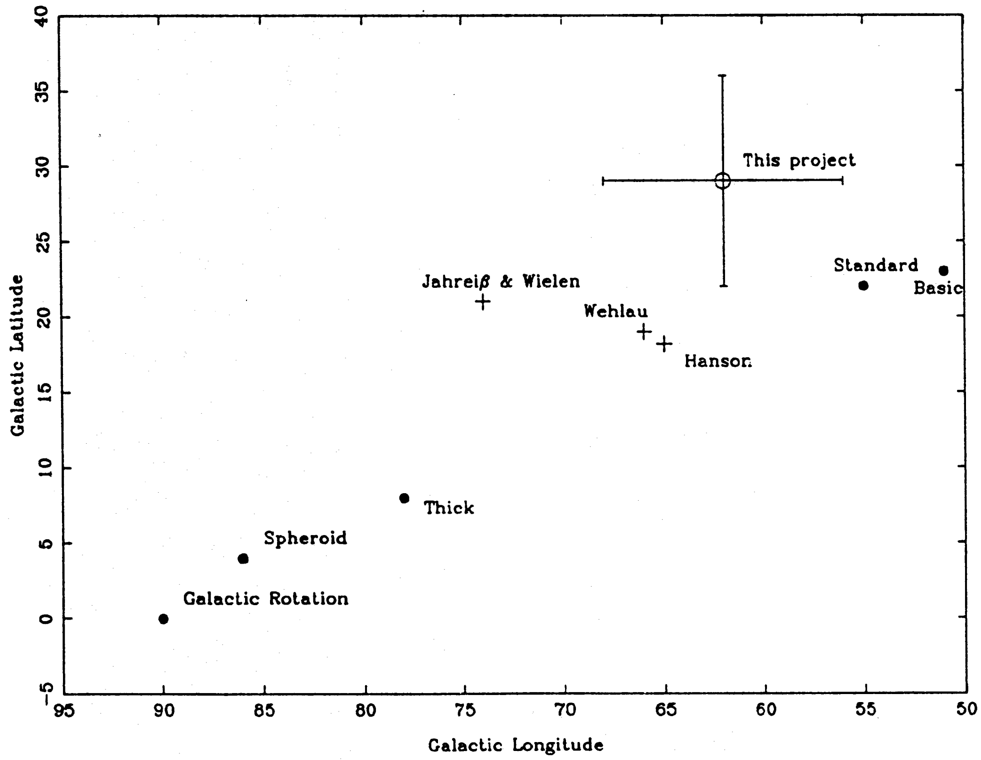

Figure 18. This diagram shows the derived solar apex for the red, $(O-E)>2.0$, stars from the four fields of the project. The bullets (●) are the expected values calculated from the basic and standard solar motions and the solar velocities used for deriving the expected RPM distributions for the thick disc and spheroid populations. The crosses (+) are similar derivations for red stars from Wehlau (1957) and Jahreiß & Wielen (1983) and for the $0° < |b| < 20°$ bin from Hanson (1987a).

were calculated to be $A = 14.4$ and $B = -12.0$ km s^{-1} kpc^{-1}. Most determinations are within ~ 3 km s^{-1} kpc^{-1} of these values but with quoted errors usually less than this, indicating that strong systematic effects are present. Since this review Dubath, Mayor & Burki (1988) have suggested that the best value for A should be 16 km s^{-1} kpc^{-1} arising from uncorrected biases in the determinations of A made from radial velocity data. This bias was also pointed out by Crézé (1970).

Other work, Clube (1973) and Fricke & Tsioumis (1975), has shown that the simple Lindblad–Oort model is not appropriate for nearby ($d \lesssim 300$ pc) stars. This cannot be tested by (or affect) this work, owing to the small number of nearby stars within the four fields. This is also one of the reasons why the stars in this analysis were restricted to distances between 200 and 1000 pc. The value for B of -26 km s^{-1} kpc^{-1} found by Clube (1973) for his distant stars is rather anomalous and is one of the few determinations close to the Oort (1972b) result of -24 km s^{-1} kpc^{-1}.

Another recent result which seemed anomalous was found in Hanson (1987a). Here the derived values were $A = 11.3$ and $B = -13.9$ km s^{-1} kpc^{-1}. However, as pointed out earlier, these values cannot be regarded as thin-disc values due to the sizeable contamination from other populations (see Lewis 1990). This is the other reason why the analysis of the current project was restricted to distances less than 1 kpc away.

A similar analysis was carried out for the blue, $(O-E) < 2.0$, stars of the project. The proper motion versus parallax plots are shown in Figs 19 and 20. No best-fitting lines are drawn to these data points due to it being very unlikely that a simple kinematic model, as used for the red stars, would be in any way appropriate. The problems here mainly stem from the inability to identify giants in the data. If no giants were present, it would be easy to limit the investigation to thin-disc stars by having a distance cut-off at 1 kpc. However, it is expected that giants will be a significant fraction of this sample of stars. The effect of this is for distant giants, which have small proper motions, to be taken as nearby stars, thus reducing the mean proper motions of these bins. This is seen in the data since hardly any of the plots have a significant gradient. Significant offsets are present in the 11-h (μ_l) and 12-h (μ_b) fields. No simple model could be found to explain the data in these plots.

9 VELOCITY DISPERSIONS

In Murray (1986) the possible explanation of the linear velocity shear in the z-direction, discovered in proper-motion data taken in the South Galactic Pole, as a consequence of the Strömberg drift, was discussed. This hypothesis was tested in this paper by investigating the velocity dispersion as a function of distance. If the velocity shear is caused by the Strömberg drift, the velocity dispersion should

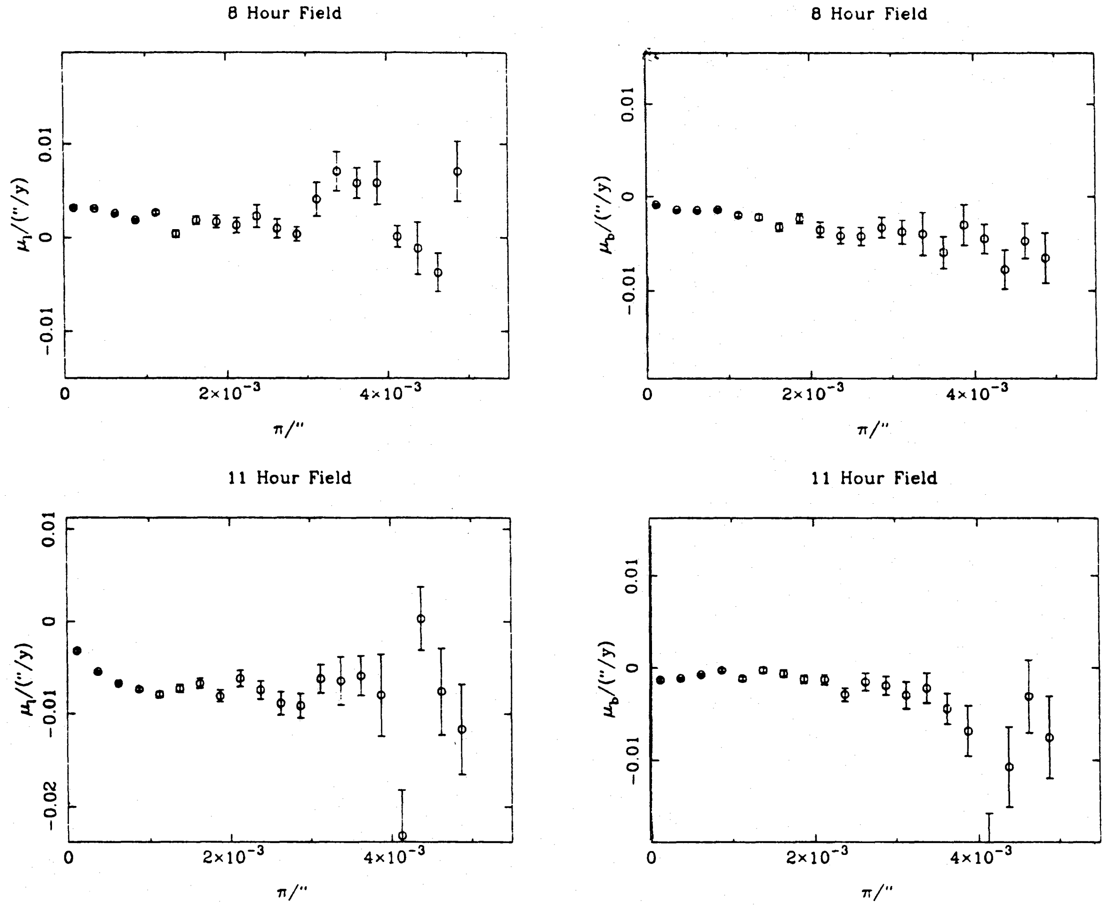

Figure 19. These diagrams show the proper motion versus parallax plots for the blue, $(O-E) < 2.0$, stars in the 8- and 11-h fields. The stars are from a central 2°-radius area of the field.

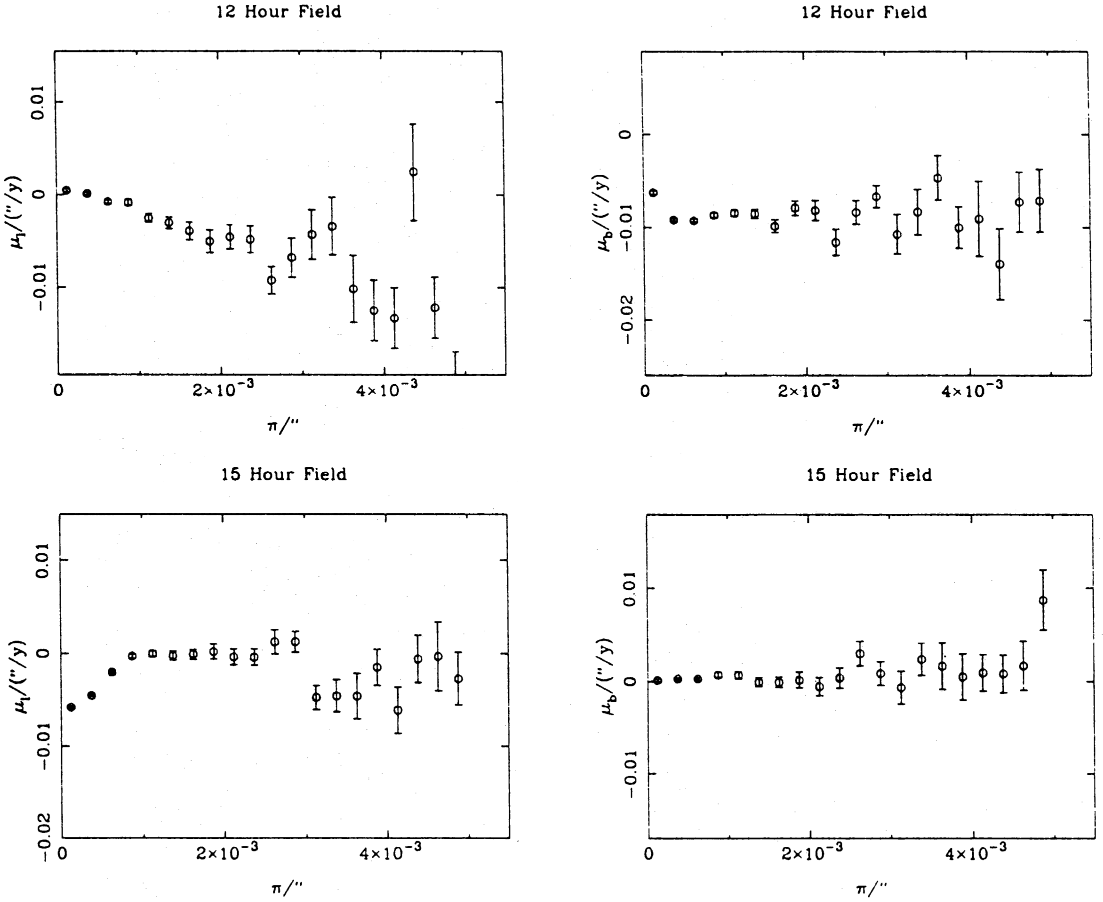

Figure 20. The same as Fig. 19 but for the 12- and 15-h fields.

increase as a function of increasing z. Although an increase was observed by Murray, it was attributed to an unknown random error in the proper motions which had not been allowed for in the determination of the velocity dispersions from the proper motion dispersions.

Since this shear was measured in the data from this project, all in the northern Galactic hemisphere, the velocity dispersion was also investigated to see if any increase was seen as a function of z. The velocity dispersion components were calculated from the following equation, which assumes that the proper motion dispersion is the quadrature sum of a contribution due to the velocity dispersion and random proper-motion errors:

$$\sigma_\mu^2 = \left(\frac{\sigma_v \pi}{4.74}\right)^2 + \sigma_{err}^2, \tag{16}$$

where σ_μ is the proper-motion dispersion in one component in arcsec yr^{-1}, σ_v the velocity dispersion in the same direction in km s^{-1}, π the parallax in arcsec and σ_{err} the random proper-motion measuring error. π was measured using photometric data, as described in the previous section, and the σ_{err} used was from table 7 of Paper I. The data was binned by parallax and the proper-motion dispersion for each bin measured. This dispersion measurement (sigma of a Gaussian distribution) was made using a quartile estimator since it is more robust than a simple root-mean-square calculation in that it is not sensitive to small contaminant populations with larger dispersions, e.g. thick disc.

Figs 21 and 22 show the projected velocity dispersions in the directions of increasing Galactic longitude and latitude as a function of parallax for the four fields of the project.

The error bars are calculated from the equation for the fractional error in a standard deviation measurement of $1/(2n-2)^{1/2}$ where n is the number of stars in the bin (Squires 1976).

Since the dispersion in proper motions due to the velocity dispersion is comparable to that arising from measurement errors, it is very important that the values used for σ_{err} are correct. This has been checked using QSO proper motions (see Section 6). In order to force the plots of Figs 21 and 22 to have a constant velocity dispersion, σ_{err} would have to be increased by more than a factor of 2, a totally unacceptable value considering these results.

As mentioned at the end of Section 5, there is a magnitude dependence to the proper-motion errors and it is important to make sure that this has not affected the velocity dispersion measurements. The proper-motion errors are quite constant down to $O=20$ mag and it is only by $O\sim21$ mag that the errors have doubled. All the parallax bins contain stars in this magnitude range, but since the dispersions are measured using a quartile estimator, which is less sensitive about the wings of the distribution, the effect of the increase in errors of the faintest objects is small.

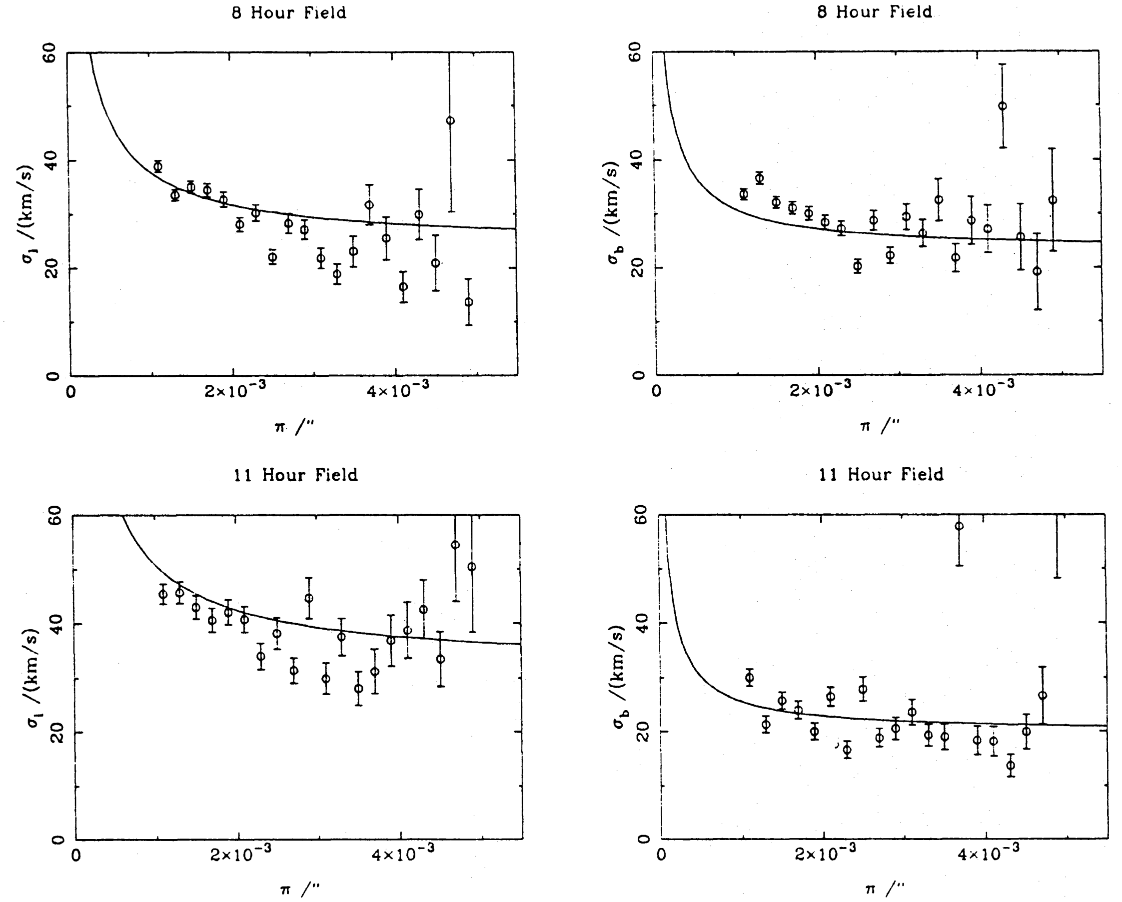

Figure 21. These diagrams show the velocity dispersion in the directions of increasing Galactic longitude and latitude as a function of parallax for red, $(O-E)>2.0$, stars in the 8- and 11-h fields. The solid line is a model based on the hypothesis that the Murray shear is due to the Strömberg drift.

To check this, the velocity-dispersion plots were recalculated using only stars with $O<20$ mag, which are unaffected by this increase. The results were very similar to those using the full sample, apart from larger random errors arising from the smaller number of objects used. This indicates that the magnitude dependence of the proper-motion errors does not affect these measurements significantly.

The model used for the predicted increase in velocity dispersion with z, as shown in these plots, is based on the relationship first found empirically by Strömberg (1924, 1925). This relationship had the functional form $v_\odot = a + b\sigma_U^2$, where $v_\odot$ is the solar motion in the V direction with respect to a particular group of stars and σ_U the velocity dispersion in the U direction for this group of stars. For the dynamical basis of this relationship see Mihalas & Binney (1983). From equation (10) it can be seen that the additional lag in the direction of Galactic rotation due to the Murray shear is equal to $-M|z|$. Therefore the velocity dispersion in the Galactic radial direction at a height z above the plane is given by

$$\sigma_U^2 = \sigma_{U_0}^2 - \frac{M|z|}{b}, \tag{17}$$

where σ_{U_0} is the U dispersion in the local neighbourhood.

The value of M used was that from Table 7 and the value of $b=0.008$ s km^{-1} is from the relationship shown in Mihalas & Binney (1983). Since the proper-motion analysis only used stars as far as 1 kpc away, this relationship should only be used in the same distance range.

Using a further dynamical relation (Mihalas & Binney 1983)

$$\frac{-B}{A-B} = \frac{\sigma_V^2}{\sigma_U^2} \tag{18}$$

and assuming that the Oort constants, A and B, do not change in the distance range considered, it is seen that σ_V must increase proportionately by the same amount as σ_U. This assumption has already been used for the Oort constant analysis.

An increasing σ_W was also considered for the model using one of the relationships given in van der Kruit (1988). Since all the fields have $b \geq 35°$, the contribution of σ_W to the observed proper-motion distributions will be small. Therefore a model with an increasing σ_W would not be easily distinguished from one with a constant σ_W, and was thus not used.

The local velocity dispersion values used were $\sigma_U=35$, $\sigma_V=25$ and $\sigma_W=20$ km s^{-1}, as used in the RPM distribution

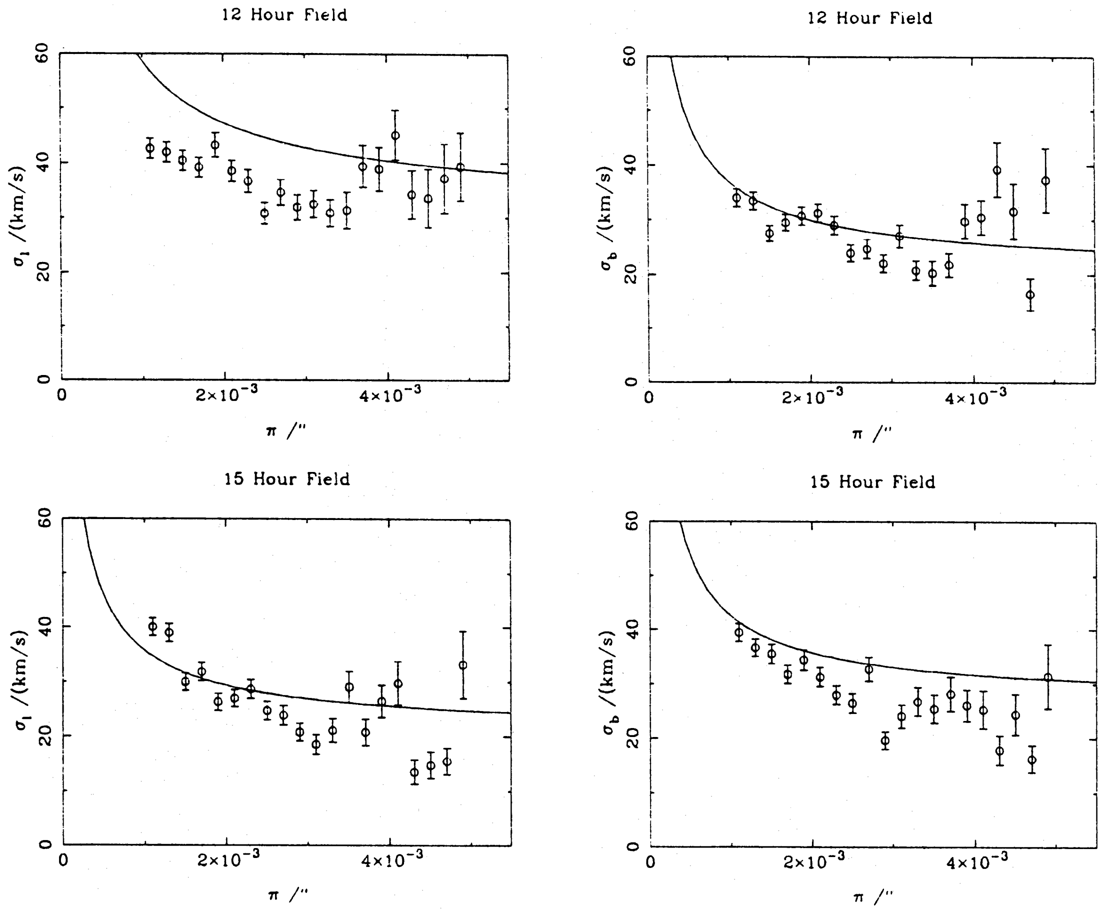

Figure 22. The same as Fig. 21 but for the 12- and 15-h fields.

calculations. After the various increases had been calculated for a particular parallax, the velocity dispersion was transformed to a Galactic normal system and projected dispersions, σ_l and σ_b, calculated from this transformed tensor in a manner described in Murray (1983).

As can be seen from these plots, this model agrees fairly well with the data. The most noticeable departure is for the σ_l plot in the 12-h field, but even then it is only about 25 per cent different. Although the predicted increase in the dispersion is not very large over the parallax range considered, the agreement with the data does suggest that the Murray shear is accompanied by an increase in velocity dispersion similar to that seen with the Strömberg drift. This is opposite to the conclusion of Murray (1986). Although there was reasonable qualitative agreement between the data and the model, no quantitative measurements were carried out. This was due to the uncertain interpretation of the effect, which led to unreliable parameters and error estimates.

Another possible reason that was considered for the Murray shear was due to the thick disc. At a height above the Galactic plane of 1 kpc (say) the effective lag is 21 km s^{-1} (see Table 7). Thick-disc stars have a lag of ~ 30 km s^{-1} with respect to the thin disc (Sandage & Fouts 1987) (SF87) which implies that if the thick disc is responsible for this shear, it must be present at 70 per cent of stars at 1 kpc. A model with a 2 per cent normalization, 1-kpc scaleheight thick disc and 300-pc scaleheight thin disc predicts ~ 20 per cent thick-disc stars at this height. This model would require a thick-disc lag of ~ 100 km s^{-1} which is in conflict with SF87. There are, however, results indicating high values for the thick-disc lag, e.g. Wyse & Gilmore (1986).

The 70 per cent fraction required by a 30 km s^{-1} lag is similar to that predicted by the density laws given by Sandage (1987), but these are not consistent with the star counts of Evans (1988). Another factor against 70 per cent thick disc at 1 kpc is that this would require much higher velocity dispersions than are observed in this data. The thick-disc velocity dispersions from SF87 are (75, 35, 42) km s^{-1} while the observed values are about 40 km s^{-1}. Therefore the thick disc probably cannot provide an explanation for the Murray shear.

10 CONCLUSIONS

The main results of our study are as follows.

(i) By careful control of systematic errors, and by using an inertial reference frame defined by a large number of background galaxies, standard Schmidt-survey photographic plates can be used reliably to generate stellar proper motions to an rms accuracy of 5 mas yr^{-1} with an absolute zero-point error of 0.6 mas yr^{-1}.

(ii) Although a reduced proper motion (RPM) diagram for the majority of faint stars on Schmidt plates lacks the discriminatory power between different Galactic models of our high proper-motion subset (Paper I), it is still possible to discern the different components of a Galactic model and thereby make use of such diagrams for selecting a certain type of stars (e.g. potential white dwarfs) for further study.

(iii) The Galactocentric peculiar velocity of the Sun was found to be (7.3 ± 1.5, 13.9 ± 2.3, 8.8 ± 2.2) km s^{-1} corresponding to the direction $l = 62° \pm 6°$, $b = 29° \pm 7°$. This result compares favourably to previous estimates. The equivalent position of the apex of the peculiar solar motion in equatorial coordinates is $17^{h}40^{m}.6 + 36°50'$.

(iv) We have derived values for the Oort's constants of $A = 19 \pm 6$ and $B = -13 \pm 5$ km s^{-1} kpc^{-1} and found a component of rotational shear at the level of -21 ± 7 km s^{-1} kpc^{-1} in the z-direction for the disc stars. This shear is similar to that observed by previous authors but somewhat smaller in magnitude, suggesting that a more complex model is needed to account for it.

(v) The trend of velocity dispersion of the disc stars as a function of z-distance was also investigated and found to compare favourably to a model first used empirically by Strömberg (1924, 1925). This suggests that the z-shear component is accompanied by an increase in velocity dispersion similar to that seen with the Strömberg drift.

ACKNOWLEDGMENTS

We thank Gerry Gilmore, Jim Lewis, Steve Maddox, Steve Warren, Richard McMahon and Matthew Colless for useful discussions and the APM group for providing such good data. DWE was financially supported for this work by SERC and Isaac Newton Studentships.

REFERENCES

Allen C. W., 1973, Astrophysical Quantities. 3rd edn. Athlone Press, London p. 125
Andersen J., 1971, A&A, 13, 40
Balona L. A., Feast M. W., 1974, MNRAS, 167, 621
Bergstrand O., 1905, Astron. Nachr., 167, 241
Bessell M. S., 1986, PASP, 98, 1303
Bowen I. S., 1960, in Kuiper G. P., Middlehurst B. M., eds, Telescopes (Stars and Stellar Systems, Vol. 1). Univ. of Chicago Press, Chicago, p. 43
Bowen I. S., 1967, QJRAS, 8, 9
Burstein D., Heiles C., 1982, AJ, 87, 1165
Charlier C. V. L., 1913, Lund Meddelanden, Serie II, 9, p. 78
Chiu L.-T. G., 1977, AJ, 82, 842
Chiu L.-T. G., 1980, ApJS, 44, 31
Clube S. V. M., 1973, MNRAS, 161, 445
Crézé M., 1970, A&A, 9, 410
Delhaye J., 1965, in Blaauw A., Schmidt M., eds, Galactic Structure (Stars and Stellar Systems, Vol. 5). Univ. of Chicago Press, Chicago, p. 61
Dubath P., Mayor M., Burki G., 1988, A&A, 205, 77
Evans D. W., 1988, PhD thesis, Univ. Cambridge
Evans D. W., 1989, A&AS, 78, 249
Evans D. W., 1992, MNRAS, 255, 521 (Paper I)
Fresneau A., 1978, AJ, 83, 406
Fricke W., Tsioumis A., 1975, A&A, 42, 449
Gunn J. E., Stryker L. L., 1983, ApJS, 52, 121
Guo X., Girard T. M., van Altena W. F., López C. E., 1993, in Morrison L. V., Gilmore G., eds, Galactic and Solar System Optical Astrometry. Cambridge Univ. Press, Cambridge
Hanson R. B., 1987a, AJ, 94, 409
Hanson R. B., 1987b, BAAS, 21, 1107
Hewitt A., Burbidge G., 1987, ApJS, 63, 1
Hinks A. R., 1898, MNRAS, 58, 428
Irwin M. J., 1985, MNRAS, 214, 575
Irwin M. J., 1994, in IAU Commission 9, Working Group on Wide-field Imaging. Newsletter 5, p. 25
Jahreiß H., Wielen R., 1983, in Philip A. G. D., Upgren A. R., eds, Proc. IAU Colloq. 76, Nearby Stars and the Stellar Luminosity Function. L. Davis Press, Schenectady, New York, p. 277
Kerr F. J., Lynden-Bell D., 1986, MNRAS, 221, 1023
Kibblewhite E. J., Bridgeland M. T., Bunclark P., Irwin M. J., 1984, in Klinglesmith D. A., ed., Proc. Astronomical Microdensitometry Conference, NASA
König A., 1962, in Hiltner W. A., ed., Astronomical Techniques (Stars and Stellar Systems, Vol. 2). Univ. of Chicago Press, Chicago, p. 461
Lewis J. R., 1990, MNRAS, 244, 247
Lindblad B., 1925, Ark. för Mat., Astron., och Fysik, 19A, 21
Linfoot E. H., 1955, Recent Advances in Optics. Clarendon Press, Oxford, Ch. 3
Menzies J. W., Banfield R. M., Laing J. D., 1980, SAAO Circulars, 1, 49
Mihalas D., Binney J., 1981, Galactic Astronomy. W. H. Freeman & Co., San Francisco
Milne E. A., 1935, MNRAS, 95, 560
Murray C. A., 1983, Vectorial Astrometry. Adam Hilger, Bristol, p. 275
Murray C. A., 1986, MNRAS, 223, 644
Murray C. A., Corben P. M., 1979, MNRAS, 187, 723
Murray C. A., Nicholson W., 1975, in de Jager, Nieuwenhuijzen, eds, Image Processing Techniques in Astronomy. Reidel, Dordrecht, Holland, p. 171
Oort J. H., 1927a, Bull. Astron. Inst. Neth., 3, 275
Oort J. H., 1927b, Bull. Astron. Inst. Neth., 4, 79
Reid N., 1990, MNRAS, 247, 70
Rufener F., Nicolet B., 1988, A&A, 206, 357
Sandage A., 1987, AJ, 93, 610
Sandage A., Fouts G., 1987, AJ, 92, 74
Shepherd W. M., 1953, MNRAS, 113, 450
Soubiran C., 1993, in Morrison L. V., Gilmore G., eds, Galactic and Solar System Optical Astrometry. Cambridge Univ. Press, Cambridge
Squires G. L., 1976, Practical Physics. McGraw-Hill, London
Straižys V., Sviderskienė Z., 1972, Bull. Vilnius Astron. Obs. No. 35
Strömberg G., 1924, ApJ, 59, 228
Strömberg G., 1925, ApJ, 61, 363
Struve L., 1987, Mémoires de l'Académie impérial de St. Pétersbourg. Ser. 7, 35, 3
Thé P. S., Steenman H. C., Alcaino G., 1984, A&A, 132, 385
van Altena W. F., Auer L. H., 1975, in de Jager, Nieuwenhuijzen, eds, Image Processing Techniques in Astronomy. Reidel, Dordrecht, Holland, p. 411
van de Kamp P., 1967, Principles of Astrometry. W. H. Freeman & Co., San Francisco
van der Kruit P. C., 1988, A&A, 192, 117
Wallace P. T., Tritton K. P., 1979, MNRAS, 189, 115
Wehlau A. W., 1957, PhD thesis, Univ. Berkeley
Wyse R. F. G., Gilmore G., 1986, AJ, 91, 855